Petroleum Science 22 (2025) 4394–4411

Contents lists available at ScienceDirect

Petroleum Science

journal homepage: www.keaipublishing.com/en/journals/petroleum-science

Original Paper

Terrestrial paleoenvironmental response of Early Eocene Climate Optimum: Implications for organic matter enrichment in the South China Sea

Jing Guo [a,b], Guang-Rong Peng [c], Fu-Jie Jiang [a,b,*], Yu-Qi Wu [a,b], Hong-Bo Li [c], Ya-Qi Li [a,b], Xin-Wei Qiu [c], Jun-Jie Cai [c], Fu-Sheng Yu [a,b], Xin Chen [c], Biao Jiang [c], Li-Shan Tang [c]

[a] State Key Laboratory of Petroleum Resources and Engineering, China University of Petroleum (Beijing), Beijing, 102249, China
[b] College of Geosciences, China University of Petroleum (Beijing), Beijing, 102249, China
[c] Shenzhen Branch, CNOOC (China) Ltd., Shenzhen, 518054, Guangdong, China

ARTICLE INFO

Article history:
Received 14 November 2024
Received in revised form
25 March 2025
Accepted 4 August 2025
Available online 11 August 2025

Edited by Jie Hao and Xi Zhang

Keywords:
Terrestrial basin
EECO record
Paleoenvironment response
Organic matter enrichment
South China Sea

ABSTRACT

The Early Eocene Climate Optimum (EECO) represents the peak of the early Paleogene greenhouse climate. However, a comprehensive understanding of the terrestrial paleoenvironmental response to the EECO and its implications for organic matter (OM) enrichment remains lacking. We integrated sedimentological, astrochronological, and geochemical data from South China Sea sediments to reconstruct the paleoenvironment and establish the OM enrichment model during the EECO. Astronomical time scales (ATS) for the Lower Wenchang Formation (Lower WC Fm.) in the Kaiping Sag, South China Sea, were established, spanning 55.4 to 43.9 Ma. During 51.5–48.7 Ma, records of astronomical signal (with overlapping cycles of 2.4 Ma, 1.2 Ma, and 405 kyr), stratigraphy (organic-rich mudstone), and paleoclimatic reconstructions (warm and humid climate) provided convincing evidence for the EECO in Kaiping Sag. This study presented the first detailed record of the terrestrial paleoenvironment response to the EECO in the South China Sea, characterized by high terrestrial input, anoxia water conditions, and elevated paleo productivity. A transient pre-warming event before the EECO exhibited a similar paleoenvironmental response, highlighting the sensitivity of terrestrial records. Post-EECO conditions showed a reversal of paleoenvironmental trends observed during the EECO. Pearson correlation analysis reveals that the EECO influenced OM enrichment by regulating paleo productivity and preservation conditions of lake. Elevated atmospheric pCO_2 levels and increased terrestrial input promoted algal blooms, thereby enhancing lake productivity. OM preservation was controlled by water column stratification and bottom water anoxia, driven by increased terrestrial input and rising lake levels. Our findings enhance the understanding of feedback mechanisms in terrestrial environments during global warming and provide insights into future climate change predictions.

1. Introduction

The Eocene epoch marks a critical transition from the Paleocene greenhouse to the Oligocene icehouse climate (Pound et al., 2017; Lauretano et al., 2021; Piedrahita et al., 2024). Within this interval, the Early Eocene (56–48 Ma) experienced the most extreme warmth of the Cenozoic era (Zachos et al., 2001, 2008; Westerhold et al., 2018), featuring superimposed transient hyperthermal events such as the Paleocene–Eocene Thermal Maximum (PETM), Eocene Thermal Maximum (ETM), and Early Eocene Climatic Optimum (EECO) (Lourens et al., 2005; Zachos et al., 2008; Bornemann et al., 2014; Varkouhi et al., 2024; Wu et al., 2025b). The EECO represents a global long-term temperature maximum in the Eocene (Bornemann et al., 2016), with reconstructed global mean temperatures exceeding modern values by > 10 °C and tropical sea surface temperatures reaching >35 °C (Hollis et al., 2012; Lunt et al., 2012; Cramwinckel et al.,

* Corresponding author.
E-mail address: jfjhtb@163.com (F.-J. Jiang).
Peer review under the responsibility of China University of Petroleum (Beijing).

https://doi.org/10.1016/j.petsci.2025.08.005

2018). This prolonged warming has been mechanistically linked to elevated atmospheric pCO_2 levels exceeding 1000 ppmv (Zachos et al., 2001, 2008; Anagnostou et al., 2016). The CO_2 vented during early Eocene volcanism in the Western Pacific, the North Atlantic Igneous Province, and the Siletzia terrane, as well as slab rollback and detachment beneath Central and East Asia, may be the responsible for EECO (Reagan et al., 2013; Cui and Schubert, 2018; Li et al., 2022a). Furthermore, methane release from the seafloor (Thomas et al., 2002; Dickens, 2011), OM oxidation (DeConto et al., 2012; Cui and Schubert, 2018) are considered to be the major contributors (Turner et al., 2014; Lauretano et al., 2015).

Currently, interpretations of temperature trends during Eocene thermal events rely on multi-site composite benthic foraminiferal isotope records compiled from multiple drill sites in various marine basins (Zachos et al., 1994, 2001, 2008; Cramer et al., 2003). These records are complemented by multi-proxy reconstructions combining sedimentology, paleontology, stable isotope geochemistry, and molecular biomarkers (Bornemann et al., 2016; Li et al., 2022a; Schaefer et al., 2022; Wang et al., 2022; Srivastava et al., 2023), providing constraints on paleoenvironmental responses during climatic extremes like the EECO. Global increased temperature will rise sea levels (Rahmstorf, 2007; Horton et al., 2008) and affect atmosphere-ocean exchange and ocean circulation (Vermeer et al., 2009; Garcia-Soto et al., 2021) during thermal events. A rise in SSTs can trigger changes in the marine ecosystem including acidification and biogeochemical perturbations (Doney et al., 2009; Gobler, 2020; Garcia-Soto et al., 2021). Moreover, the organic-rich shale exhibits a negative $\delta^{13}C_{org}$ isotope excursion ascribed to recycling of ^{13}C-depleted organic matter (OM) via upwelling attributed to a transient thermal event (Schaefer et al., 2022).

Terrestrial systems exhibited pronounced feedbacks to Eocene thermals through coupled hydrological and biogeochemical responses. Near-equatorial regions likely maintained tropical rainforest resilience via enhanced water-use efficiency under elevated precipitation regimes (Srivastava et al., 2023), while Central Asian arid zones experienced proto-monsoonal greening that facilitated mammalian dispersal corridors (Wing et al., 1991; Meijer et al., 2024). Mid-latitude Basins such as Bohai Bay Basin recorded elevated lake levels during the MECO (Shi et al., 2020; Wu et al., 2025a), evidenced by sedimentological proxies indicating humid conditions, freshwater influx, and stratified water columns. Additionally, the environmental response to these thermal events was reflected in enhanced silicate weathering and increased terrestrial debris input (Hyland and Sheldon, 2013; Dzombak and Sheldon, 2022). The prolonged greenhouse climate could have contributed to carbon cycle feedbacks by promoting organic carbon burial in terrestrial basins (Shi et al., 2019; Fan et al., 2024; Liu et al., 2024a; Wu et al., 2024; Yin et al., 2024). The OM accumulation in the Green River Formation was associated with low-oxygen, nutrient-rich, alkaline saline environments during the EECO (Hyland et al., 2013; Pommer et al., 2023). Comprehensive analyses suggests that paleoclimate-driven environmental changes were the primary factors influencing variations in organic-rich fine-grained sediments in the Fushun Basin (Li et al., 2021, 2022a). Wu et al. (2025a) proposed that the MECO drove paleoenvironmental fluctuations, including a warm and humid climate, increased water depth, reduced salinity, anoxic conditions, and elevated atmospheric pCO_2 levels, which led to OM enrichment in the Shahejie Formation of the Bohai Bay Basin, China. Furthermore, the role of astronomical forcing in Eocene thermal events and the formation of organic-rich sediments in mid to high-latitude regions has been extensively validated (Shi et al., 2021; Li et al., 2022a; Wei et al., 2023; Liu et al., 2024). However, the lack of terrestrial records from low-latitude regions regarding the EECO event and its influence on OM enrichment currently limits our understanding of the global thermal climate and carbon cycle during the Eocene.

The organic-rich mudstones of the lower member of the Wenchang Formation (lower Mbr. WC Fm., 56.5–43.9 Ma) in the Kaiping Sag of the Pearl River Mouth Basin were continuously deposited during the Early Eocene, providing an ideal stratigraphic record of the EECO (Peng et al., 2023; Xu et al., 2024). This study aims to address the existing knowledge gap by presenting multiple lines of evidence to offer a comprehensive understanding of the paleoenvironmental conditions during the EECO. Astrochronological analysis was employed to establish the high-resolution age of the lower Mbr. WC Fm. Based on elemental geochemical characteristics and global comparisons with marine foraminiferal isotopic data, Paleoclimate reconstructions were used to identify the geological record of the EECO in Kaiping Sag. Total organic carbon (TOC) and rock pyrolysis indicators were utilized to assess the degree and type of OM enrichment. Furthermore, Pearson correlation coefficient analysis was applied to determine the key controlling factors of OM enrichment during the EECO, and its geological model was established. Understanding the terrestrial paleoenvironmental response and OM enrichment during the EECO is crucial for reconstructing past climate conditions and informing strategies to address future climate change.

2. Geological setting

The Pearl River Mouth Basin is a low-to mid-latitude, petroleum-bearing basin located at the junction of the Eurasian, Pacific, and India-Australia plates (Fig. 1(a), Ye, 2019). It features a structural configuration of three uplift zones and two depression zones arranged in a north-south orientation (Fig. 1(b), Ma, 2020). The Kaiping Oilfield, situated within the basin, is China's first deep-water oilfield, with proven geological reserves of 102 million tonnes of oil equivalent, setting a national record for deep-water petroleum testing production (Yin, 2024). The Kaiping Sag consists of five sub-Sags, covering an area of 6000 km^2, with a water depth of approximately 300 m (Fig. 1(b), Cai et al., 2023). Cenozoic stratigraphy reflects the influence of tectonic movements and displays a “land-to-sea” transition (Peng et al., 2023). The Eocene Wenchang (WC Fm.) and Enping formation (EP Fm.) consist of continental deposits resting on a Paleogene volcanic basement, overlain by the marine Zhuhai Formation from the Oligocene (Fig. 1(c), Gao et al., 2024a). The WC Fm. is subdivided into upper (Mbr. 1, Mbr. 2, and Mbr. 3) and lower (Mbr. 4, Mbr. 5, and Mbr. 6) members (Peng et al., 2023; Xu et al., 2024). The boundary between the lower Mbr. WC Fm. and the upper Mbr. WC Fm. in Kaiping Sag is dated at 43.9 Ma (Peng et al., 2023; Xu et al., 2024). The organic-rich and thick mudstones of lower Mbr. WC Fm. serve as the primary source rocks, providing substantial petroleum reserves for the Kaiping Sag (Cai et al., 2023; Peng et al., 2023).

3. Methodology

3.1. Sampling and experiments

The organic-rich mudstone of the Wenchang Formation (WC Fm.) was the ideal formation for studying Eocene thermal events and the carbon cycle during these events. To minimize potential diagenetic influence on the elemental geochemical records, we chose and conducted experiments on mudstones from well W3, located in the uplift of Kaiping Sag. The lower member of the Wenchang Formation (lower Mbr. WC Fm.) in Well W3 is located beneath the seafloor, between 3368 m and 4115 m, and consists of shale, mudstone, and sandstone with varying grain sizes. Combined with the age anchor of 43.9 Ma (boundary age between the

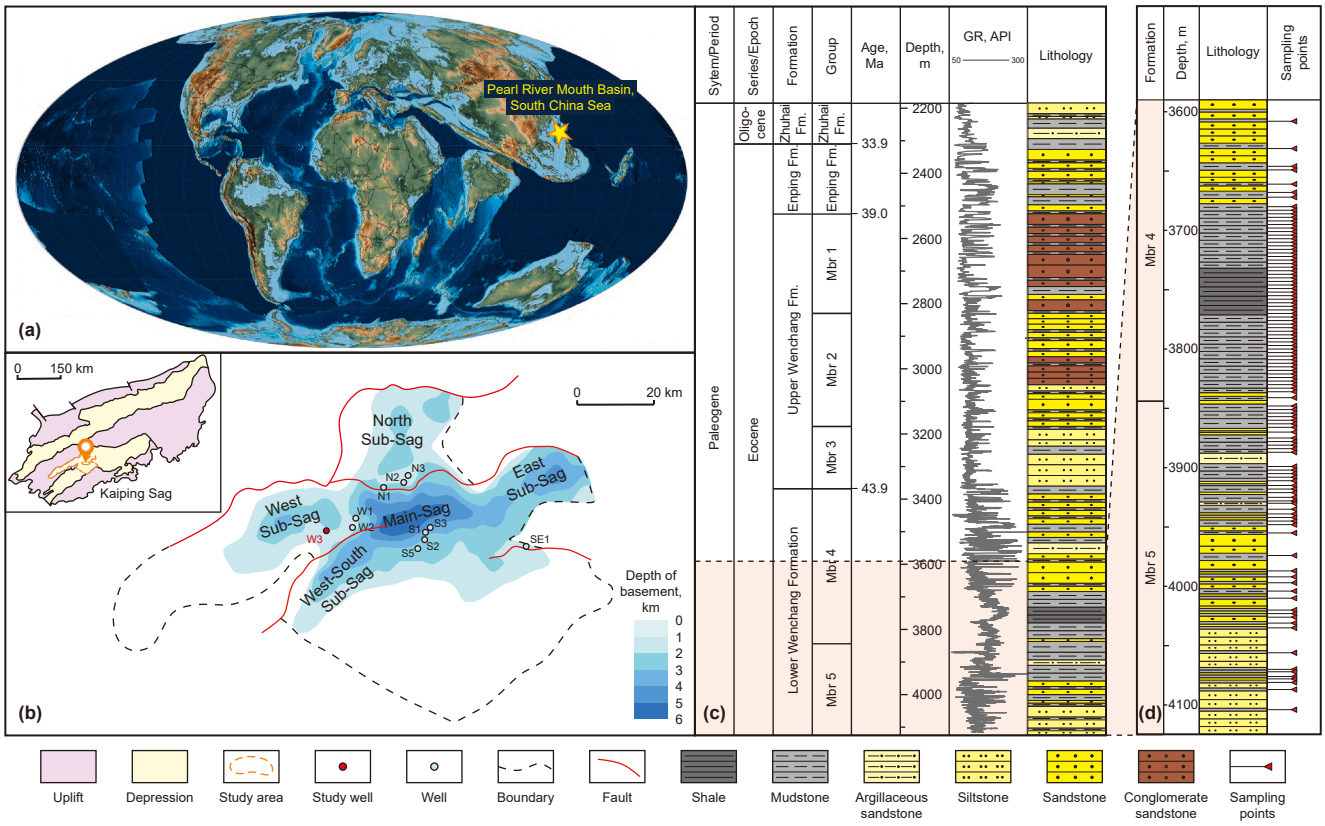

Fig. 1. **(a)** Paleogeographic evolution of Paleogene of 52.2 Ma and the location of Pearl River Mouth Basin (Modified from Scotese, 2014; Ma et al., 2020). **(b)** The location and tectonic division of the Kaiping Sag and location of sampling well (Modified from Peng et al., 2023). **(c)** Stratigraphic characteristics of well W3, Kaiping Sag. Stratigraphy, age, thickness, GR data, and lithology of the Eocene strata are described (Provided by Shenzhen Branch, CNOOC). **(d)** The 110 sampling points of well W3.

upper and lower WC Fm.), the lower Mbr. WC Fm. GR curve of Well W3 was conducted astrochronological analysis, aiming to establish astronomical time scales (ATS). Based on the ATS of lower Mbr. WC Fm. and the ages of thermal events, we selected 110 mudstone samples from Well W3 (as shown in Fig. 1(d)), which span the early Eocene interval, including the ETM and EECO climate. Specially, the high-precision sampling was conducted between 3680 and 3870 m of sediment deposited during the EECO period, with an average sampling interval of approximately 3 m. These 110 samples were conducted X-ray fluorescence (XRF) elemental analysis, TOC content determination, and Rock-Eval analysis to investigate responses to climate events in terrestrial basins. All of experiments were conducted from the Shenzhen Branch, CNOOC.

XRF is one of the most commonly used techniques for chemical elemental analysis (Hu, 2013). This method determines the elemental composition of minerals by analyzing the secondary X-rays emitted when rocks are irradiated with high-energy electrons or charged ions (Liang, 2007; Hu, 2013). XRF analysis allows for the determination of concentrations of various elements, including Mg, Al, Si, S, P, K, Ca, Ba, Ti, Mn, Fe, and Sr. XRF measurements can achieve precision up to five decimal places. This method is distinguished by its rapid analysis time, minimal sample size requirements, low particle size specifications for rock samples, high analytical precision, and straightforward experimental procedures. Prior to analysis, 110 samples from Well W3 were crushed, with approximately 10 g selected from each sample. We measured the instrument error of the XRF analyzer by performing 20 consecutive measurements on the same sample from the same region. The calculated measurement error for the elements was ±0.03%. While this result shows some discrepancy compared to traditional experimental measurements, it is still within an acceptable range.

The LECO CS-230 carbon-sulfur analyzer is used to determine TOC content. Following the GB/T 19145-2022 standard procedure (Standardization Administration, 2022), samples are ground to a 200-mesh size, treated with hydrochloric acid to remove inorganic carbon, and then rinsed with distilled water for neutralization. The pretreated samples are then tested using the instrument. The Rock-Eval II instrument is employed for pyrolysis experiments on rock samples. When samples are heated to 300 °C in the pyrolysis instrument, the spectral peak area corresponds to the volatile hydrocarbons (S_1) content. The spectral peak area from heating the sample from 300 °C to 600 °C reflects the content of pyrolytic hydrocarbons (S_2). The peak of S_2 is associated with the maximum pyrolysis peak temperature (T_{max}). The hydrogen index is calculated as the ratio of S_2 to TOC content.

3.2. Astrochronological analysis

Gamma ray (GR) records provide high-resolution sedimentary cyclicity for continuous stratigraphy. The GR series curves from the lower Mbr. WC Fm. in the Well W3, ranging from 3368 to 4115 m, were used for astrochronological analysis. Prior to analysis, raw GR data from 3368 to 4115m were standardized for a unified series, which was detrended by subtracting a 35% weighted average to remove the long-term trend ($GR_{detrened}$) (Cleveland, 1979; Torrence and Compo, 1998). Linear interpolation was applied to the GR data to achieve an average sampling interval of 0.1 m. The data were then re-evaluated using a Locally Weighted Scatterplot Smoothing (LOESS). The 2π multi-taper method (MTM) was used

for power spectral analysis (Thomson, 1982), estimating the robust red noise spectrum and identity significant frequencies that exceed the 95% confidence level (Mann and Lees, 1996; Meyers, 2015) to detect potential orbital cycles. According to the astronomical solutions from La2010 and La2004, the main cycles identified in the Paleogene include 405, 125, 95, 54, 39.3, 23.1, 21.9, and 18.8 kyr (Laskar et al., 2004, 2011). Frequency ratio method was applied to the data set to test for the presence of astronomical frequencies (Boulila, 2019; Wang et al., 2020). And we utilized evolutionary Fast Fourier transform (FFT) spectrograms to inspect the evolution of frequencies through the succession (Kodama and Hinnov, 2014). The Correlation Coefficient (COCO) was used to estimate the optimal sedimentation rate (Li et al., 2018a; Wang et al., 2020; Huang et al., 2023a), assessing sedimentation rates ranging from 0.1 to 20 cm/kyr with a step size of 0.1 cm/kyr through 5000 Monte Carlo simulations.

The 405 kyr eccentricity cycle, recognized as the most stable astronomical period of the Phanerozoic, can be used to establish stratigraphic timescales (Laskar et al., 2004, 2011; Huang et al., 2023a). Gaussian bandpass filtering (Kodama and Hinnov, 2014) was applied to isolate eccentricity, obliquity, and precession cycles in the GR data. Based on the calculation of optimal sedimentation rate and using the 405 kyr long eccentricity as a calibration standard, we conducted an astronomically tuned analysis and depth-time conversion to determine the floating astronomical time scales for the lower Mbr. WC Fm. The age of lower Mbr. WC Fm. will be calculated by combining the age anchor with the floating astronomical time scales. The above numerical analyses were performed using Acycle 2.8 software.

3.3. Paleoclimate reconstruction

Elemental geochemical indicators are commonly used to reconstruct paleoclimate. The Rb/Sr ratio is an effective indicator of paleoclimate, with an increase in the Rb/Sr ratio representing greater humidity and enhanced weathering (Roy and Roser, 2013). The Mg/Ca ratio is positively correlated with temperature: high Mg/Ca values correspond to a hot and dry climate and low values correspond to a humid/warm climate (Morford and Emerson, 1999). The *C* value (*C* value=(Fe + Mn + Cr + V + Ni + Co)/(Ca + Mg + Sr + Ba + K + Na)) of fine-grained mudstones is also an effective indicator of paleoclimate (Guo et al., 2020). In humid climates, sedimentary rocks tend to have higher contents of elements such as Fe, Mn, Cr, V, Ni, and Co. Conversely, during dry climates, evaporation causes the precipitation of Ca, Mg, K, Na, Sr, and Ba on the bottom of the water (Hu et al., 2017). A high *C* value suggests a warm and humid climate (Moradi et al., 2016). Lake level changes reflect the response of lakes to paleoclimate variations (Woolway et al., 2020). Clay minerals are relatively rich in elements such as Fe, while Ti is predominantly found in sandstone (Zhang et al., 2011; Hu, 2013). The Fe/Ti ratio indicates changes in the grain size of lacustrine sediments, thereby reflecting fluctuations in lake levels (Marshall et al., 2011; Cui et al., 2019).

3.4. Paleoenvironment reconstruction

Ti and Al are representative elements that indicate detrital input in sedimentary rocks (Calvert and Pedersen, 2007; Wang et al., 2014; Murphy et al., 2000). The Sr/Ba ratio reflects changes in water column salinity, with values below 0.6 indicating freshwater conditions (Wei and Algeo, 2019). The trace elements V and Cr are sensitive indicators of paleo redox conditions. Low V/Cr ratios represent an anoxia environment (Jones and Manning, 1994; Algeo and Lyons, 2006). Enhanced organic C (OC) preservation at lower redox conditions and enhanced sedimentary retention of remineralized organic P (OP) at higher redox conditions results in a strong relationship between benthic redox conditions and sedimentary C_{org}/P (C_{org}/P=(TOC/12)/(P/30.95)) (Algeo and Ingall, 2007). C_{org}/P values delineate three redox conditions: values below 50 represent oxic conditions, values between 50 and 100 represent hypoxic conditions, and values above 100 represent anoxia conditions (Algeo and Li, 2020). Phytoplankton contribute OC and OP to sediments, enabling the elemental P content to serve as a qualitative indicator of paleo productivity (Guo et al., 2020). The P/Al ratio is utilized to assess levels of paleo productivity while accounting for the effect of terrestrial input (Algeo and Scheckler, 1998). Moreover, Fe is an essential nutrient for algal growth (Redfield, 1960; Schenau et al., 2005; Dong et al., 2023) and is used as a key indicator of lake productivity.

3.5. Pearson correlation analysis

Prior to analysis, data were screened for accuracy. Extreme outliers were identified using *Z*-scores (Eq. (1): X = measured values, $\widehat{X}$ = average value, σ = standard deviation), with values greater than ±3 considered outliers and subsequently removed from the dataset (Potter et al., 2019). We assessed the assumptions necessary for Pearson correlation analysis. The normality of the distributions for both variables was examined using Shapiro-Wilk tests (Mishra et al., 2019). The presence of linear relationships (Weisburd et al., 2020) was visually inspected via scatterplots, and no significant deviations were observed.

$$Z=\frac{X-\widehat{X}}{\sigma} \tag{1}$$

The pearson correlation coefficient was employed to quantify the linear relationship strength between the organic enrichment degree (TOC) and the paleoenvironment (including paleo climate, paleo water depth, redox conditions and paleo productivity). This coefficient (r) was calculated using Eq. (2) (Weisburd et al., 2020). The X and Y are the measured values, and $\widehat{X}$ and $\widehat{Y}$ are the respective means of the samples.

$$r=\frac{\sum(X-\widehat{X})(Y-\widehat{Y})}{\sqrt{\sum(X-\widehat{X})^2\sum(Y-\widehat{Y})^2}} \tag{2}$$

The significance of the correlation coefficient was tested using a two-tailed *t*-test (Weisburd et al., 2020). The null hypothesis H_0 assumed no correlation between the variables ($\rho = 0$), while the alternative hypothesis H_α suggested a non-zero correlation. The test statistic was calculated as Eq. (3). Where r is the sample correlation coefficient, n is the sample size (110 samples), and the degrees of freedom were $(n - 2)$. The correlation was considered statistically significant if the resulting p-value (2.648) was less than the predetermined significance level of $\alpha = 0.01$. All statistical analyses were conducted using MATLAB software.

$$t=\frac{r\sqrt{n-2}}{\sqrt{1-r^2}} \tag{3}$$

4. Results

4.1. Astronomical time scales (ATS)

Spectral analysis of the Well W3 $GR_{detrended}$ revealed the presence of various statistically significant peaks, all of which exceed the 95% confidence level (Fig. 2(a)). The ratio of peaks at wavelengths of 27.1, 8.8, 6.2, 3.4, 2.4, 1.5, 1.4, and 1.2 m was 22:7:5:3:2:1.2:1.1:1, consistent with the ratio of the target astronomical cycle (22:7:5:3:2:1.2:1.1:1). The results of COCO analysis showed that the significance level of the null hypothesis was <0.01 (Fig. 2(b); H_0: no astronomical forcing). The strongest correlation occurs at a sedimentation rate of 6.4 cm/kyr, which is within the range of sedimentation rates (6–18 cm/kyr) for the Wenchang Formation in the Pearl River Mouth Basin (Wei et al., 2020, 2023), as determined by previous astronomical tuning studies, and is also close to the optimal sedimentation rate for source rocks in terrestrial basins (Zhao et al., 2022). The correlation was strongest at a sedimentation rate of 6.4 cm/kyr. Therefore, we identified 6.4 cm/kyr as the optimal sedimentation rate for Lower Mbr. WC Fm. (Fig. 2(b)). Based on the interpretation of the average sedimentation rate, the frequency component centered on 1/27.1 m was extracted using a Gaussian bandpass filter. This signal is calibrated to the 405 kyr long eccentricity. The calibrated GR power spectral cycles were 405 kyr (405 long eccentricity), 131 kyr (125 short eccentricity), 93 kyr (95 short eccentricity), 51 kyr (54 Obliquity), 36.6 kyr (39.3 Obliquity), 22.9 kyr (23.1 precession), 20.6 kyr (21.9 precession), and 18.2kyr (18.8 precession), similar to the target astronomical cycle (Laskar et al., 2011; Fig. 2(a)). Two other robust spectral peaks occur before the frequency of 0.1 cycle/m, attributed to the 1.2 Myr (Laskar et al., 2004; Boulila et al., 2011; Fig. 2(c)) and 173 kyr long modulating obliquity cycles (Boulila et al., 2018; Zhang et al., 2022a). A robust spectral peak occurs at the frequency of 0.0062 cycle/m, attributing to the long modulating eccentricity cycles (~2.4 Myr) (Boulila et al., 2011; Olsen et al., 2011; Fig. 2(c)). According to the 405kyr calibration, a floating ATS of the formation was calculated. Age (43.9 Ma) of the upper Mbr. WC Fm. and lower Mbr. WC Fm. boundary in the Kaiping Sag (Fig. 1(c)) is used as an anchor for our floating astronomical time scale. The ATS of the lower Mbr. WC Fm. was 55.4–43.9 Ma (Fig. 2(d): Tuned GR). The established ATS falls in the range of 56.5 to 43.9 Ma calculated by previous studies (Gao et al., 2024a, 2024b; Xu et al., 2024), confirming the validity of the astronomical analysis in this study. This interval spans the 109th to 135th 405 kyr eccentricity cycles (E109–E135) of the La2010 astronomical solution (Laskar et al., 2011; Fig. 2(d)).

4.2. Elemental geochemical characteristics

The elemental contents obtained by XRF analysis are shown in the Supplementary Material. They are normalized according to PAAS (Post-Archean Australian Shale), as shown in Fig. 3. Elemental contents are influenced by the mineral composition of the rocks. The major elemental contents of 110 samples are dominated by Si and Al. The Si content ranges from 20.98% to 35.04%, with an average of 29.30%. The Al content varies between 6.80% and 14.52%, with an average of 10.56%. The Fe content ranges from 1.71% to 9.47%, with an average of 5.47%. The Ca content varies between 0.10% and 6.02%, with an average of 0.91%. Compared to marine sediments, terrestrial rocks exhibit a relatively low Mg content (Hu, 2013). Specifically, the Mg content in the lower Mbr. WC Fm. ranges from 0.06% to 0.81%, with an average of 0.32%. The Na and P content of the Lower Mbr. WC Fm. mudstones varied widely, ranging from 0.02% to 2.68% and 0.001%–0.11%. The contents of K and Ti range from 1.13% to 3.46% and from 0.15% to 0.80%, respectively, while the Mn content ranges from 0.024% to 0.135%. The contents of Si, Al, Fe, K, Ti, and Mn in the WC Fm. are similar to the contents of PAAS, while there is a significant depletion of Mg (Fig. 3(a)).

In the PAAS-normalized spider diagram, the distribution of Ca, Na, and P differs between samples (Fig. 3(a)). The distribution of most trace elements in Lower Mbr. WC Fm. mudstones in the Kaiping Sag were similar to that in the PAAS (Fig. 3(b)). The contents of V (avg. 0.008%), Ni (avg. 0.003%), Cu (avg. 0.006%), Zn (avg. 0.015%), Sr (avg. 0.011%), Ba (avg. 0.073%), Th (avg. 0.003%), U (avg. 0.001%), Zr (avg. 0.029%), and Rb (avg. 0.021%) are all below 1.0%. The Ba content ranges from 0.055% to 0.176%, making it a significant component of the trace elements. The Ni and Sr in the samples are widely distributed, while Cu and Th exhibit a more concentrated distribution (Fig. 3(b)).

4.3. Paleoclimate indicators

Based on paleoclimate characteristics of Kaiping Sag, we divided the sedimentation periods into 3 stages (Fig. 6). Stage I (55.0–51.5 Ma) is characterized by a Rb/Sr range of 0.64–4.04, with an average of 1.14; Mg/Ca values between 0.05 and 0.76, averaging 0.32; and *C* values ranging from 0.59 to 1.82, with an average of 1.18. Notably, significant peaks in Rb/Sr, Mg/Ca, C value, and Fe/Ti appear at approximately 53.2 Ma, 53.8 Ma, 54.5 Ma, and 52.5–52 Ma, indicating abrupt fluctuations in climate (Fig. 6). In stage II (~51.5–48.7 Ma), the Rb/Sr ratio ranges from 0.47 to 8.24, with an average of 3.45; Mg/Ca values vary between 0.20 and 1.63, averaging 0.83; and *C* values range from 0.47 to 3.33, with an average of 2.07. Paleoclimate indicators are significantly higher than in other stages, suggesting a prolonged warm and humid climate during this period (Fig. 6). In stage III (48.5–47.5 Ma), the paleoclimate experienced a sudden cooling, with an average Rb/Sr ratio of 3.15, an average Mg/Ca ratio of 0.44, and an average *C* value of 0.40.

4.4. Paleoenvironmental indicators

Table 1 presents the range and average values of three stages of paleoenvironmental indicators recorded in the lower Mbr. WC Fm. source rocks, encompassing paleo water depth, terrestrial inputs, paleo salinity, redox condition, and paleo productivity (Table 1). In Stage I, the paleoenvironment exhibited fluctuating changes, characterized by a significant fluctuation in Fe/Ti ratios, Ti contents, Al contents, Sr/Ba ratios, V/Cr ratios, C_{org}/P, Fe contents, and P/Al ratios (Table 1). In stage II, the Fe/Ti values range from 9.10 to 20.08, averaging 14.99, indicating that paleo water depth was markedly higher than in other stages. The characteristics of the stage II are the Ti contents, Al contents, Sr/Ba ratios, V/Cr ratios, C_{org}/P, Fe contents, and P/Al ratios reaching stability, with average values of 0.43, 12.26, 0.13, 2.10, 1765.32, 6.43, and 0.0008, respectively (Table 1). Stage III is also characterized by a decline in lake levels, terrestrial inputs, paleo salinity, redox conditions, and paleo productivity as indicated by an average Fe/Ti ratio of 9.48, Ti contents of 0.20, Al contents of 8.14, Sr/Ba ratios of 0.16, V/Cr ratios of 2.39, C_{org}/P ratios of 580.27, Fe contents of 1.87, and P/Al ratios of 0.0003 (Table 1). Detailed data are available in the supplementary materials.

4.5. Source rock evaluation

The OM abundance, type, and maturity are commonly used to assess the quality of source rocks (Tissot and Welte, 1984). The TOC content of 110 samples ranges from 0.50% to 12.48%, with an average of 3.55%. The S_1+S_2 values range from 0.62 to 51.88 mg/g,

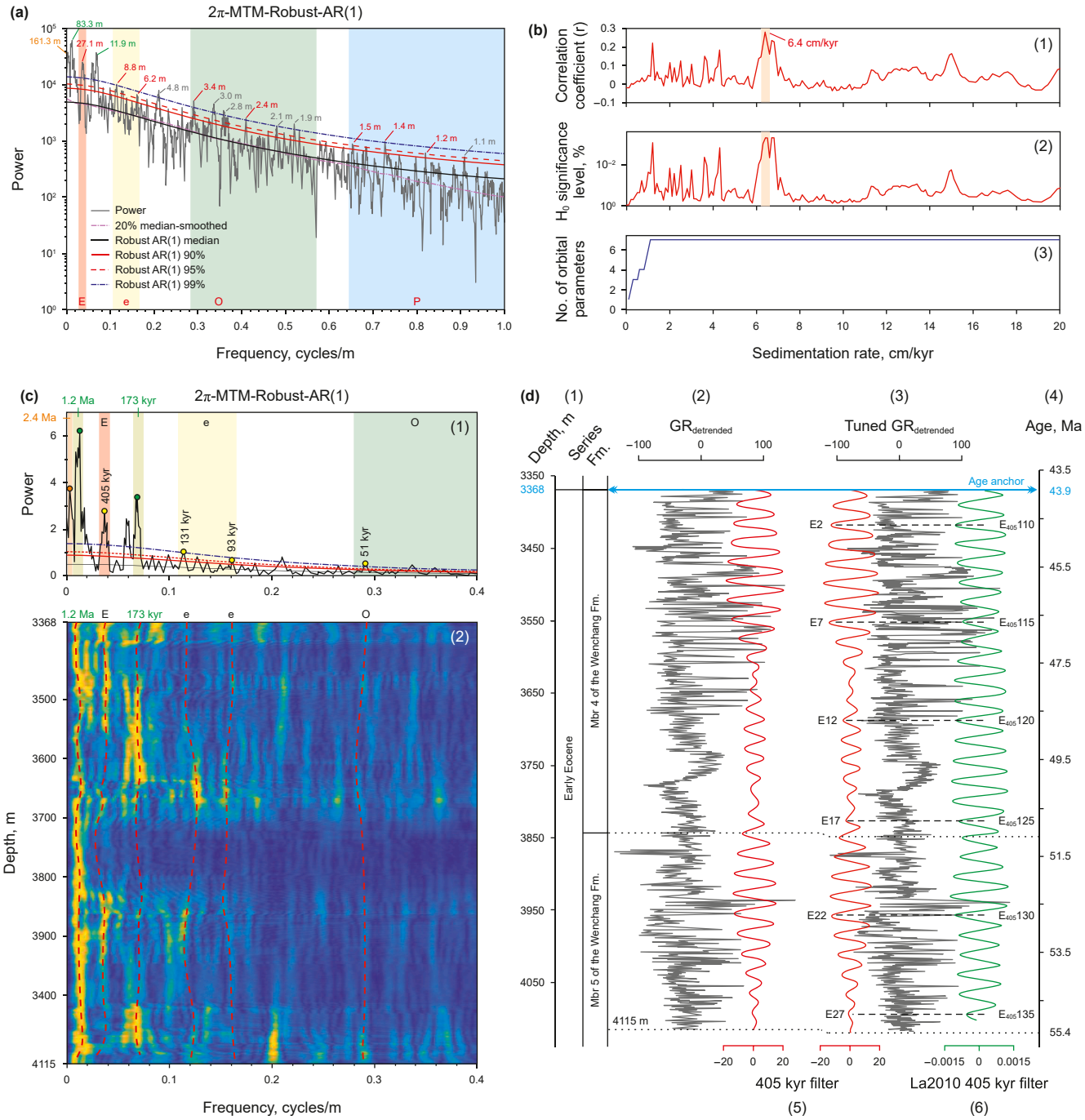

Fig. 2. Interpretation cyclic stratigraphy of Well W3 gamma ray series from the Kaiping Sag. **(a)** 2π MTM power spectra of selected GR series is shown with background AR (1) model, 90%, 95%, and 99% confidence levels. Robust AR (1) model and different confidence levels show significant peaks (red words), which are marked with the inverse of frequency, E: Long eccentricity (red), e: short eccentricity (yellow), O: Obliquity (green), P: Precession (blue). The yellow and green words represent the wavelength of the long eccentricity modulation cycle and obliquity modulation cycles recorded in the GR series, while the gray words represent the wavelength of other cycles. **(b)** COCO analysis: (1) correlation coefficient, (2) null hypothesis and H_0 significance level (H_0: no astronomical forcing), and (3) number of contributing astronomical parameters. The sedimentation rate test from 0.1 to 20 cm/kyr with steps of 0.1 cm/kyr. The optimum deposition rate calculated by COCO analysis is 6.4 cm/kyr **(c)** (1) 2π MTM power spectra and (2) evolution fast fourier transform of selected GR series. The shaded area shows the filter bandwidth of long eccentricity (2.4 Ma, 405 kyr), short eccentricity (131 kyr, 91 kyr), and obliquity (1.2 Ma, 173 kyr, 51 kyr). The 2.4 Ma (yellow dot) represents the long eccentricity modulation cycle recorded in the GR series, while 1.2 Ma and 173 kyr correspond to obliquity modulation cycles (green dots). The red dashed lines represent the long eccentricity, short eccentricity, and obliquity cycles. **(d)** Composite histogram of Well W3, featuring (1) depth, (1) formation, (2) GR detrended data, (3) tuned GR detrended curves, (5) filtered output, and (4) absolute time scale. The absolute time scale is anchored at 43.9 Ma (blue line) at the top of the Lower Member of the Wenchang Formation. The 405 kyr long eccentricity filters are presented in a red (this study) and (6) green curve (La2010 model). Earth' s orbital parameters from 55.4 to 43.9 Ma presented in ETP format according to the La2010 model (Laskar et al., 2011).

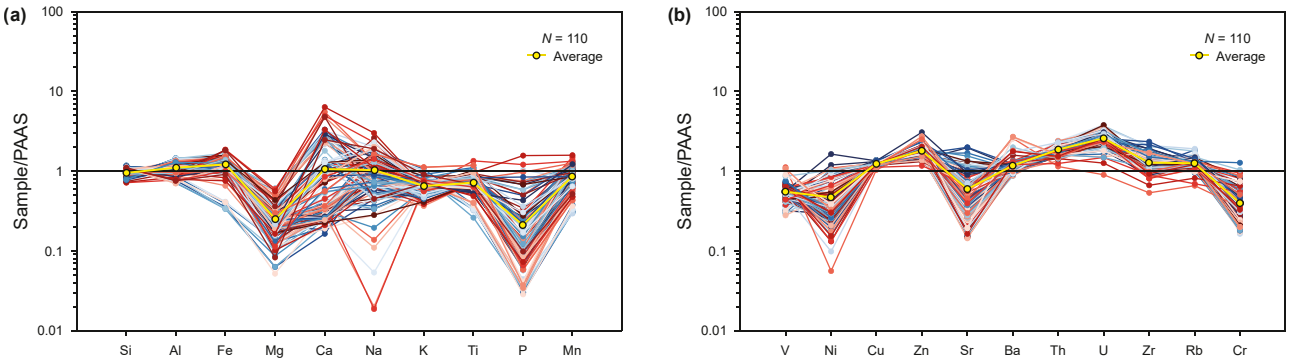

Fig. 3. Standardized spider web map of elements. **(a)** Major elements map of the lower Mbr WC Fm. **(b)** Trace element map of the lower Mbr WC Fm. mudstones standardized by PAAS (PAAS data from Hu and Gao, 2008). The yellow dots were the average values of 110 samples standardized by PAAS.

Table 1
Paleoenvironmental indictors of the lower Mbr. WC Fm.

Stage	Environment	Paleo water depth	Terrestrial inputs		Paleo salinity	Redox condition		Paleo productivity	
	Indictor	Fe/Ti	Ti	Al	Sr/Ba	V/Cr	C_{org}/P	Fe	P/Al
I	Range	7.11–16.80	0.29–0.80	7.00–12.93	0.02–0.34	0.74–7.32	31.83–2137.62	3.82–9.47	0.0004–0.0130
	Avg.	12.98	0.53	9.20	0.14	2.89	481.12	6.27	0.0026
II	Range	9.10–20.08	0.23–0.57	8.01–14.52	0.04–0.53	0.73–4.55	287.49–6968.85	2.06–8.41	0.0002–0.0035
	Avg.	14.99	0.43	12.26	0.13	2.10	1765.32	6.43	0.0008
III	Range	8.32–10.81	0.16–0.23	7.09–9.14	0.06–0.26	1.96–2.78	435.83–691.17	1.71–2.08	0.0002–0.0004
	Avg.	9.48	0.20	8.14	0.16	2.39	580.27	1.87	0.0003

with an average of 13.27 mg/g. In Stage I, the values of S_1+ S_2 and TOC exhibit frequent fluctuations, suggesting significant heterogeneity in OM abundance of source rocks (Fig. 4(a) and (b)). The S_1+S_2 and TOC in Stage II show consistently high values, whereas in Stage III, S_1+ S_2 and TOC are significantly lower (Fig. 4(a) and (b)). More than 72% of the samples fall within the great-excellent category (Fig. 4(b)). It is noteworthy that T_{max} exhibits a peak near a depth of 3850 m (Fig. 4(a)). Except for four abnormally high values (distributed around "$R_o \approx 1.2\%$" in Fig. 4(c)), the range of T_{max} is 422–456 °C, with an average value of 446 °C. The HI values range from 92 to 414 mg/g, with an average of 304 mg/g. The vertical trend of the HI values is similar to S_1+S_2 and TOC (Fig. 4 (a)). The Van diagram is a commonly used tool for distinguishing kerogen types (Tissot and Welte, 1984; Van Krevelen, 1993). The kerogen types of the lower Mbr. WC Fm. source rocks are classified as Type I and Type II (Fig. 4(c)). Most samples fall within Type I, indicating that the OM sources of the lower Mbr. WC Fm. mudstone are primarily derived from phytoplankton and algae. All samples exhibit a vitrinite reflectance (R_o) greater than 0.5%, indicating that they have entered the oil window (Fig. 4(c)).

5. Discussion

5.1. Age model

The selection of age anchor and the establishment of ATS are critical for identifying thermal events and documenting associated environmental responses. As early as the 1990s, previous studies established a biostratigraphic framework for the Pearl River Mouth Basin, assigning the Wenchang Formation to the Early Eocene (Hao et al., 1996; Huang and Zhong, 1998; Huang, 1999; Agnini et al., 2014; Qin, 2000). Subsequent research by Shao et al. (2017) compared detrital zircon U-Pb geochronology records from ocean drilling sites in the South China Sea with boreholes data from the Pearl River Mouth Basin, constraining the age of the Wenchang Formation to 65–38 Ma (Shao et al., 2017). Zhang et al. (2020) further refined this age to approximately 39–55 Ma by integrating micropaleontological evidence, detrital zircon dating, and palynological climate data from the Pearl River Mouth Basin, correlated with global tectonic and climatic events (Zhang et al., 2020). Seismic data indicate that the T83 seismic interface marks the sequence boundary between the upper and lower Mbr. WC Fm (Shi et al., 2020; Gao et al., 2023; Yang et al., 2023). The lower Mbr. WC Fm. in the Kaiping Sag is predominantly composed of lacustrine mudstone interbedded with thin sandstone and siltstone layers. In contrast, the upper Mbr. WC Fm. exhibits coarser-grained lithologies (Xiong, 2021). By combining seismic interface of T83 with abrupt changes in GR curves and lithological variations, the stratigraphic boundary between the upper and lower Mbr. WC Fm. was identified at a depth of 3368 m in well W3 (Fig. 5(a) and (b)). This stratigraphic division is consistent with stratigraphic results from other wells in the Pearl River Mouth Basin (Xiong et al., 2021; Huang et al., 2023b).

The thermal history of source rocks and fission track age indicates a significant increase in temperature and geothermal flow values around 44 Ma, which corresponds closely with the magmatic peak interval identified by Shi et al. (2020) between 43.3 and 41.1 Ma (Guo et al., 2007; Li et al., 2018b; Shi et al., 2020). Considering the spatial heterogeneity of the sags, Shi et al. (2020) estimated the boundary age between the upper and lower Mbr. WC Fm. to be approximately 43 Ma, based on the sedimentation rates (Shi et al., 2017, 2020). Previous studies have linked this boundary age (the T83 interface at 43 Ma) to the Huizhou tectonic Movement, based on tectonic changes in increased fault activity, and magmatic activity (Zhang et al., 2022c; Huang et al., 2023b). Nie et al. (2021) recalculated the main parameters of the structural subsidence in the Kaiping Sag, adjusting the previously proposed 43 Ma for the T83 interface to 43.9 Ma. The boundary age of 43.9 Ma is now widely accepted and applied in various studies (Peng et al., 2023; Gao et al., 2024a, 2024b; Xu et al., 2024a, 2024b). Furthermore, the age of 43.9 Ma is close to the C20n magnetochron in GTS2020 (43.45 Ma, Dinarès-Turell et al., 2018; Speijer et al.,

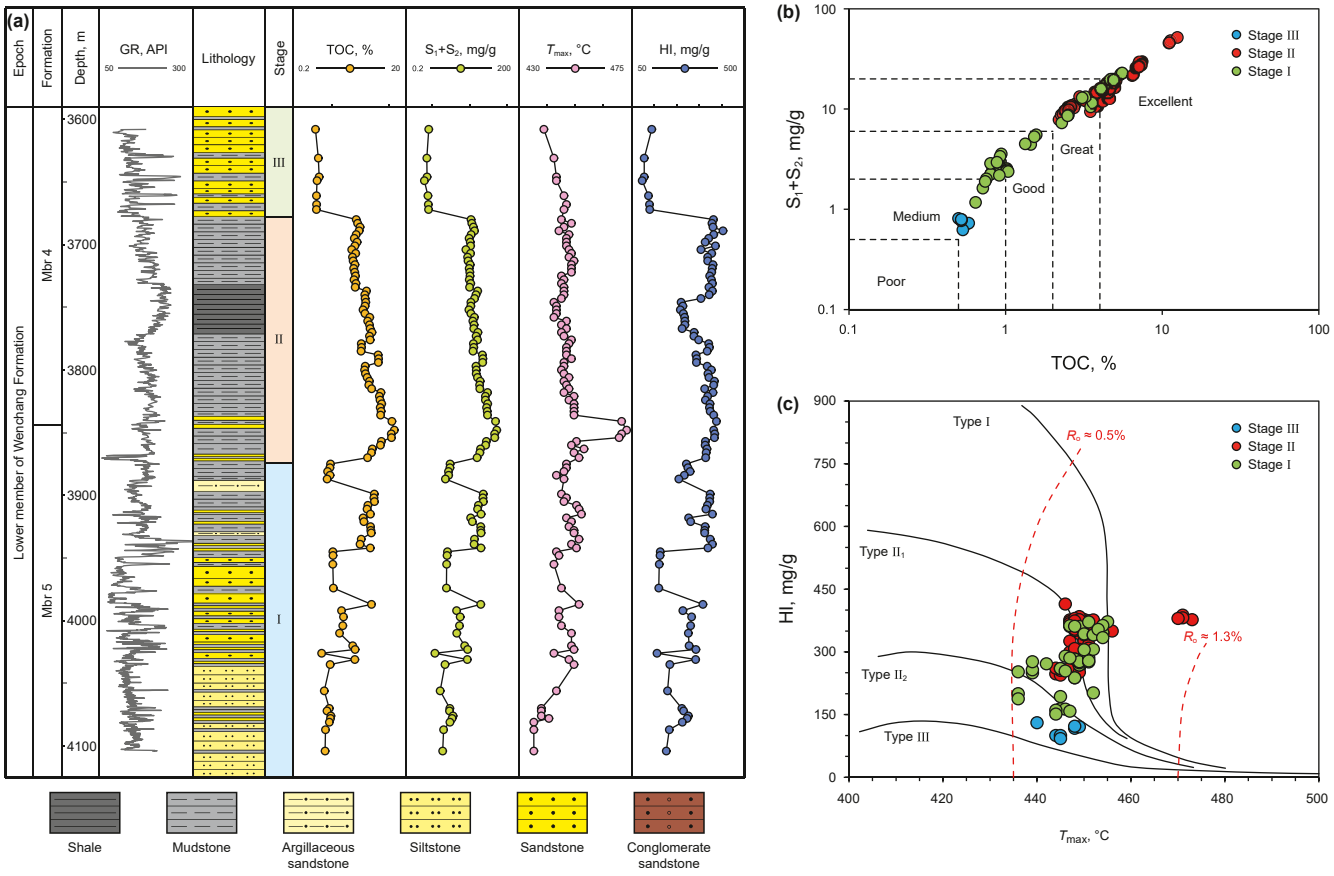

Fig. 4. Evaluation of source rocks in the Lower Mbr. WC Fm. in Kaiping Sag. **(a)** Vertical organic geochemical characteristics. **(b)** Evaluation of OM abundance (the template is adapted from Xiong et al., 2021). **(c)** Classification of OM types (the template is adapted from Schaefer et al., 2022).

2020). Therefore, 43.9 Ma was selected as the age anchor for astronomical tuning in this study. The results show that the sedimentary strata between 3368 and 4115 m span 27 long eccentricity cycles, with the ATS ranging from 43.9 to 55.4 Ma (Fig. 2(d)). The established ATS falls within the previously calculated range of 56.5 to 43.9 Ma (Gao et al., 2024a, 2024b; Xu et al., 2024a), confirming the validity of the astronomical analysis in this study.

5.2. Records of Early Eocene Climate Optimum (EECO)

5.2.1. Regional availability of indicators

In lacustrine sediments, Rb and Sr originate from two sources: one is the rock fragments (parent rock) transported and deposited through physical weathering, while the other is dissolved materials brought in through chemical weathering, which often precipitates in carbonate forms (Zeng et al., 2011). To accurately interpret the Rb and Sr content, it is crucial to exclude the influence of carbonate minerals, as they can distort the elemental data (Wei and Algeo, 2019; Li et al., 2020). This study establishes a relationship between the Rb/Sr ratio and Ca content to assess the validity of using the Rb/Sr ratio as a paleoclimate indicator (Fig. 6(a)). The analysis shows that when the Ca content is below 0.5%, there is no correlation between the Rb/Sr ratio and Ca content. However, when the Ca content exceeds 0.5%, the linear relationship between Rb/Sr and Ca becomes weak, with an R^2 value of 0.05 (Fig. 6(a)). This indicates that in the Kaiping Sag, the Rb/Sr ratio is not influenced by carbonate rocks, making it a reliable indicator for paleoclimate reconstruction. Similarly, the Sr/Ba ratio is important to account for the influence of carbonates (Ca, %) on Sr contents. The correlation between Sr/Ba and Ca content ($R^2 = 0.03$ when Ca> 0.5%) indicates that the Sr/Ba remains a valid indicator for paleo salinity (Fig. 6(b)). Thus, both the Rb/Sr and Sr/Ba ratios can be used effectively to reconstruct past climatic and environmental conditions in the Kaiping Sag.

5.2.2. Identification of EECO

Global Eocene strata (52–48 Ma) document significant climatic events, including the PETM (~56 Ma) (McInerney and Wing, 2011), ETM 2 (~54.5 Ma) and ETM3 (~53.2 Ma) (Li et al., 2022a), and the EECO (52–49 Ma) (Srivastava et al., 2020). The ATS (55.4–43.9Ma) of lower Mbr. WC Fm. in the Kaiping Sag spans the early Eocene, including the ETM and EECO. The ETM is characterized by rapid atmospheric temperature increases of approximately 3–5 °C and carbon isotopic excursions ranging from approximately 1‰–6‰, reflecting substantial perturbations to the global carbon cycle (Zachos et al., 2001, 2008). In contrast, the EECO represents a prolonged interval of peak global warmth, marked by sustained high temperatures and negative oxygen isotopic excursions occurring at 52–49 Ma (Zachos et al., 2001, 2008; Crouch et al., 2020; Srivastava et al., 2020). After the EECO, the Earth experienced a gradual transition into a prolonged cooling trend, which persisted through the mid-late Eocene (Zachos et al., 2001, 2008; Katz et al., 2008; Bijl et al., 2010). The continuous sedimentary record preserved in the Kaiping Sag offers a valuable opportunity to investigate terrestrial responses to these global climatic events during the Early Eocene.

Marine oxygen and carbon isotope variations have long been utilized as a global reference framework for identifying climate

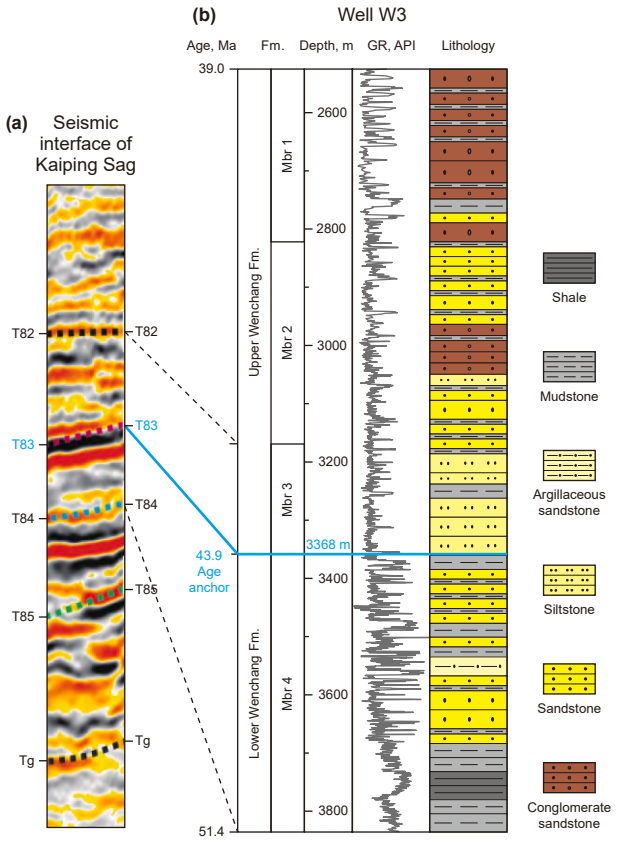

Fig. 5. Age model and stratigraphic lithology. **(a)** The seismic interface of Wenchang Fm., Kaiping Sag (modified from Gao et al., 2023); T83 represents the seismic interface of upper and lower WC Fm (blue words). **(b)** Stratigraphic lithology histogram of Well W3, Kaiping Sag (this study); the boundary age between the lower Mbr. WC Fm. and the upper Mbr. WC Fm. in Kaiping Sag is 43.9 Ma (blue words).

events preserved in sedimentary records. In this study, we use the oxygen and carbon isotope dataset from deep-sea benthic foraminifera spanning the past 66 Ma, compiled by Westerhold et al. (2020), to correlate global climate fluctuations with terrestrial records from the Kaiping Sag. Previous studies have shown that the deposition of organic-rich rocks often temporally coincides with thermal events (e. g. Schaefer et al., 2022), suggesting a strong link between climate perturbations and terrestrial sedimentation processes.

In Stage I, the Kaiping Sag experienced three distinct transient warming episodes at ~54.5 Ma, ~53.8 Ma, and ~53.2 Ma. These intervals are marked by peaks in climate-sensitive geochemical proxies, including Rb/Sr, Mg/Ca, and *C* values, along with the deposition of organic-rich sediments. These warming intervals correspond to globally recognized events: ETM2, J, and ETM3 events, respectively, and are further supported by coeval carbon and oxygen isotopes excursions in marine strata (Sluijs et al., 2009; Stap et al., 2010; Li et al., 2022b). Between 52.5 and 52 Ma, short-term isotope excursions (~0.5 Myr) in the lower Mbr WC Fm. coincide with TOC enrichment, suggesting another warming interval. From ~51.5 to 48.7 Ma, benthic foraminiferal oxygen isotopic excursions of approximately 1‰ (Fig. 7) indicate a temperature increase of about 4 °C, during which approximately 200 m of continuous organic-rich mudstone and shale (TOC> 2.5%) accumulated in the Kaiping Sag. This period shows significant negative oxygen isotope excursions and positive carbon isotope excursions (Fig. 7(a)–(c)), indicating sustained warm conditions. This warming interval in Stage II corresponds to the EECO event. However, the terrestrial record from the Kaiping Sag shows an earlier onset and longer duration of warming (~52.5–48.7 Ma) than that inferred from marine records (~52–49 Ma) (Zachos et al., 2008; Srivastava et al., 2020). This earlier and more prolonged warming in terrestrial strata suggests a heightened sensitivity of continental environments to global climate forcing (Li et al., 2022a, 2022b; Wu et al., 2025a). The period from 52.5 to 52 Ma is defined in this study as the Sub-EECO, a prelude to the EECO warming. The geochemical evidence for warming (Rb/Sr, Mg/Ca, *C* values), elevated TOC content, and Fe/Ti ratios also indicate increased precipitation and lake-level rise (Fig. 7(e)), consistent with sea-level trends observed during the EECO and with records from other basins such as the Bohai Bay Basin during the MECO (Shi et al., 2019; Wu et al., 2025a).

Furthermore, astronomical modulation appears to play a crucial role in driving these climate perturbations (Huang et al., 2014; Wang et al., 2020). In the GR log of Well W3, spanning 43.9–55.4 Ma, we identify a long eccentricity modulation cycle of 2.4 Ma and a long obliquity modulation cycle of 1.2 Ma (Fig. 2(c)). The minima of these two modulation cycles coincide temporally with the minimum of the 405 kyr eccentricity (Fig. 7(d)), forming a convergence of orbital minima known to be associated with major climate disruptions, such as the Cretaceous Oceanic Anoxic Events (OAEs) and the middle Miocene global cooling (Abels et al., 2005; Mitchell et al., 2008).

Although the warming onset indicated by geochemical proxies slightly lags behind the astronomically defined start of the EECO,

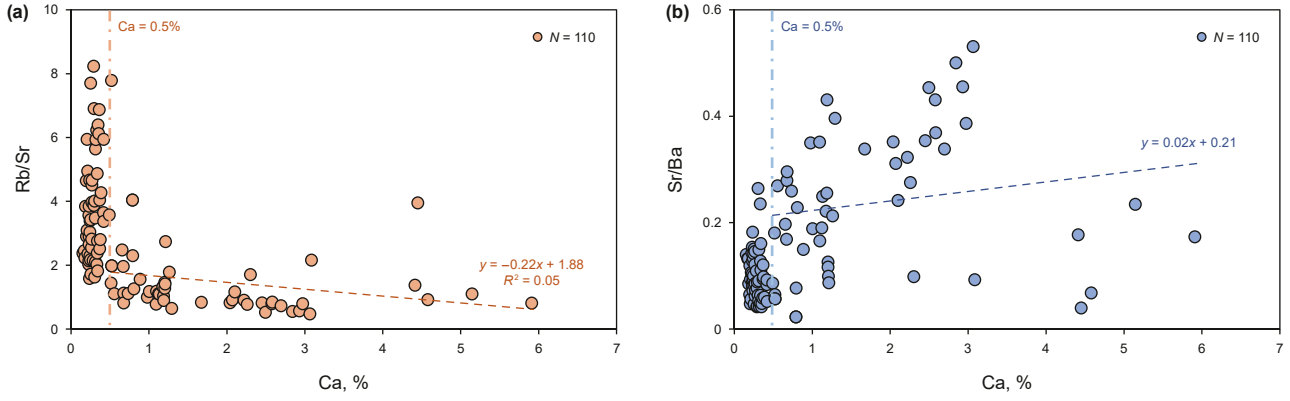

Fig. 6. Identification of the effectiveness of Sr elements for paleo climate and paleo salinity reconstruction. **(a)** The Rb/Sr vs. Ca plot showed that the paleoclimate of 110 samples is not affected by carbonate rocks. **(b)** The Sr/Ba vs. Ca plot showed that the paleo salinity of 110 samples is not affected by carbonate rocks.

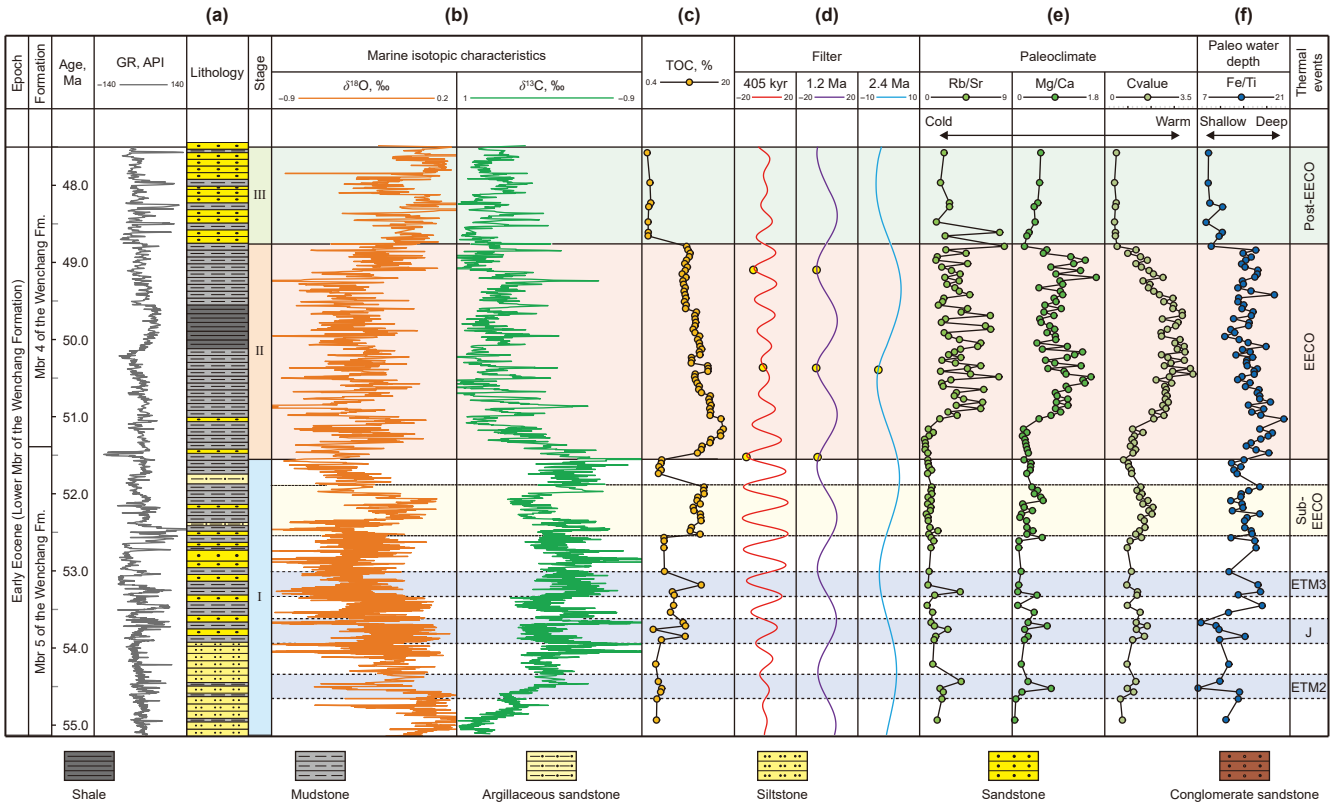

Fig. 7. Records of Early Eocene climatic events in the lower Mbr. WC Fm., Kaiping Sag. **(a)** Lithology of the lower Mbr. WC Fm.; **(b)** Oxygen and carbon isotope variations in deep-sea benthic foraminifera from 55 Ma to 47.5 Ma (Data from Westerhold et al., 2020). **(c)** TOC content in the lower Mbr. WC Fm. mudstones. **(d)** Eccentricity and obliquity filtering recorded in the gamma ray (GR) curve of the lower Mbr. WC Fm.; the red curve represents the stable 405 kyr long eccentricity filter; the purple curve represents the 1.2 Ma modulated obliquity filter; and the blue curve represents the 2.4 Ma long modulated eccentricity filter; the yellow dots represent the minimum overlap of these filters. **(e)** Reconstructed Early Eocene paleoclimate based on Rb/Sr, Mg/Ca, and *C* values. **(f)** Reconstructed Early Eocene paleo water depth based on Mn/Ti. The different color shadings indicate various climatic events recorded in the Kaiping Sag, with the blue shading specifically representing the ETM events.

the synchronicity of organic-rich sediment deposition, isotopic signals, and evidence of terrestrial environmental response justify defining the EECO interval in the Kaiping Sag as 51.5–48.7 Ma. Additionally, the alignment of ETM event ages with sedimentary and isotopic markers further supports the robustness of the terrestrial geological record as a high-resolution archive of global climatic events.

Although the warming onset indicated by geochemical proxies slightly lags behind the start of the EECO we have defined, the synchronicity of organic-rich rock deposition, isotopic signals, the evidence of terrestrial environmental response, and astronomical signals justify defining the EECO interval as 51.5 to 48.7 Ma in the kaiping Sag. In addition, the alignment of ETM events ages with sedimentary and isotopic signals further confirm the reliability of the geological record associated with the EECO.

5.3. Paleoenvironmental response of EECO

The thermal events during the Early Eocene, particularly the EECO, led to significant changes in the sedimentary and biogeochemical characteristics of the Kaiping Sag, providing insights into the paleoclimate, lake conditions, and biological activity during this period (Liu et al., 2017). By comparing the paleoenvironmental response before, during, and after the EECO, several key aspects of climate and ecosystem changes can be observed (Figs. 6 and 7).

Before the EECO event (Sub-EECO: ~52.5–52 Ma), the climate exhibited a pre-warming stage (Figs. 7 and 11(a)), with transient increases in Rb/Sr, Mg/Ca, and C values (Fig. 7(e)). This period also witnessed positive feedbacks in the Mn/Ti ratios, which indicate rising lake levels (Fig. 7(f)). This short-term climate warming resulted in enhanced weathering and increased terrestrial input (Fig. 8(c)), contributing nutrients and influencing the lake's ecological dynamics. Paleo salinity, paleo-redox conditions, and paleo productivity exhibited positive feedback (Fig. 8(d)–(f)), characterized by increases in Sr/Ba, C_{org}/P, Fe, and P/Al, along with a decrease in V/Cr. This stage was characterized by high OM abundance (TOC: average 4.43%), primarily from algae and phytoplankton (HI: average 345 mg/g) (Fig. 8(a) and (b)), suggesting that the increased biological activity was linked to the higher nutrient availability from terrestrial inputs.

During the EECO, the Kaiping Sag experienced a warm and humid climate, with high lake levels (Fig. 7), as indicated by the consistent patterns of increased Rb/Sr, Mg/Ca, C values, and Mn/Ti ratios. The warming is further supported by a low-latitude mechanism involving obliquity-driven changes in the cross-equatorial insolation meridional temperature gradient (Bosmans et al., 2015). These changes would have influenced rainfall, continental weathering rates, and surface runoff, which contributed to the enrichment of nutrients in the lake (Li et al., 2016; Srivastava et al., 2023; Liu et al., 2024b). The lake during this period remained freshwater, with Sr/Ba values consistently below 0.6 (Fig. 8(d)). As the climate warmed and precipitation increased, the lake's salinity remained stable (Sr/Ba around 0.09), likely facilitating OM accumulation in a more tranquil environment. During the EECO, the long-term decrease in V/Cr and the sustained increase in C_{org}/P indicate that the Kaiping Sag experienced anoxia

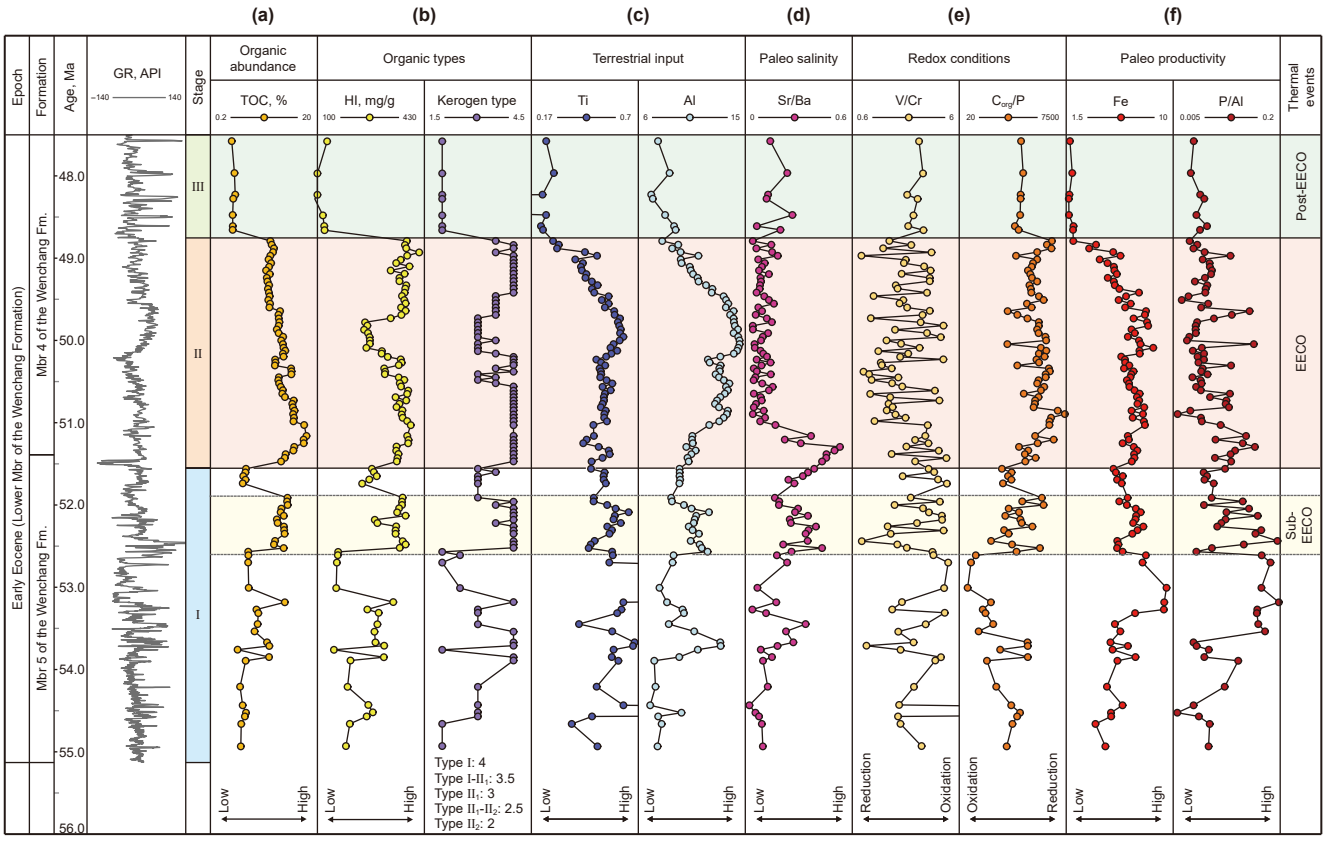

Fig. 8. Paleoenvironmental evolution profile recorded in the lower Mbr. WC Fm., Kaiping Sag, before, during, and after the EECO. **(a)** OM abundance in mudstone (TOC). **(b)** OM types in mudstone, including HI content and results from Van's classification. **(c)** Early Eocene terrestrial input reconstructed from Ti and Al contents. **(d)** Early Eocene paleo salinity reconstructed from Sr/Ba ratios. **(e)** Early Eocene redox conditions reconstructed from V/Cr and C_{org}/P ratios. **(f)** Early Eocene paleo productivity reconstructed from Fe and P/Al ratios. Arrows at the bottom of the evolution profile indicate the paleoenvironmental significance of each indicator. Shadings of yellow, red, and green represent the environmental evolution before (Sub-EECO), during (EECO), and after the EECO (Post-EECO), respectively.

water condition (Fig. 8(e)). This, in turn, fostered the growth of aquatic organisms, including algae and phytoplankton, as reflected by the elevated HI and consistent presence of Type I kerogen (Fig. 8 (b)). Elevated paleo productivity (Fig. 8(f)) further supporting the idea that phytoplankton and algae blooms were linked to increased terrestrial nutrient input.

After the EECO (Post-EECO: ~48.7–47.5 Ma), the climate underwent a rapid cooling and a declined lake level, marked by a decline in Rb/Sr, Mg/Ca, *C* value, and Fe/Ti (Figs. (7) and 11(b)). The cooling trend is corresponding to positive oxygen isotopic excursions of benthic foraminifera (Fig. 7(e)). The reduction in Ti and Al contents indicates a decrease in terrestrial input (Fig. 8(c)), possibly as a result of diminished precipitation and runoff. The redox conditions during the post-EECO became more oxidized, as indicated by the increase in V/Cr and C_{org}/P ratios, suggesting less anoxic conditions compared to the EECO (Fig. 8(e)). The decrease in productivity is further supported by lower Fe content, P/Al ratio, TOC, and HI (Fig. 8), indicating that the lake nutrient pool was depleted, resulting in reduced organic matter accumulation. This indicates that the paleoenvironment in the Kaiping Sag had shifted toward a more nutrient-poor state following the EECO, marking the onset of cooler and less biologically productive conditions.

5.4. OM enrichment mechanism during the EECO

5.4.1. Assess the key factors controlling OM enrichment

Previous studies have demonstrated that the degree of OM enrichment is primarily controlled by the redox conditions and paleo productivity (Demaison and Moore, 1980; Parrish, 1995; Ingall and Jahnke, 1997; Algeo and Tribovillard, 2009). To identify the key factors controlling OM enrichment in the Kaiping Sag during the EECO, we conducted a correlation analysis of 110 samples, focusing on paleoclimate, paleo water depth, terrestrial input, OM sources, redox conditions, paleo productivity, and TOC content. Our results show that the average TOC content during the EECO was 4.68%, significantly higher than the overall average of 3.55% across 110 samples (Fig. 9). This period coincided with the warmest climate conditions (Fig. 7). As the *C* value increased, TOC content showed a logarithmic growth trend (Fig. 9(a)). The relationship between TOC and paleo water depth, as well as redox conditions, exhibited exponential growth (Fig. 9), suggesting that elevated lake levels and anoxia environments facilitated OM preservation, with enrichment reaching its peak during the EECO. Previous studies indicate that increased terrestrial input can enhance water flow rates, promoting rapid OM deposition. However, when sedimentation rates exceed a certain threshold, excessive terrestrial inputs may dilute the OM concentration. Our findings show that TOC content increase with rising terrestrial input, a peak, and then declines, a trend also observed in other terrestrial basins, such as the Bohai Bay Basin (Hu et al., 2021; Wu et al., 2024). The point at which TOC content begins to decline represents the threshold of maximum OM enrichment, which is influenced by lacustrine conditions. In the Kaiping Sag, TOC contents rise and fall with increasing terrestrial input, reaching a peak at an Al content of 4.45% (Fig. 9(c)). A positive correlation between TOC and HI (Fig. 9(d)) indicates that OM type is a key indicator of

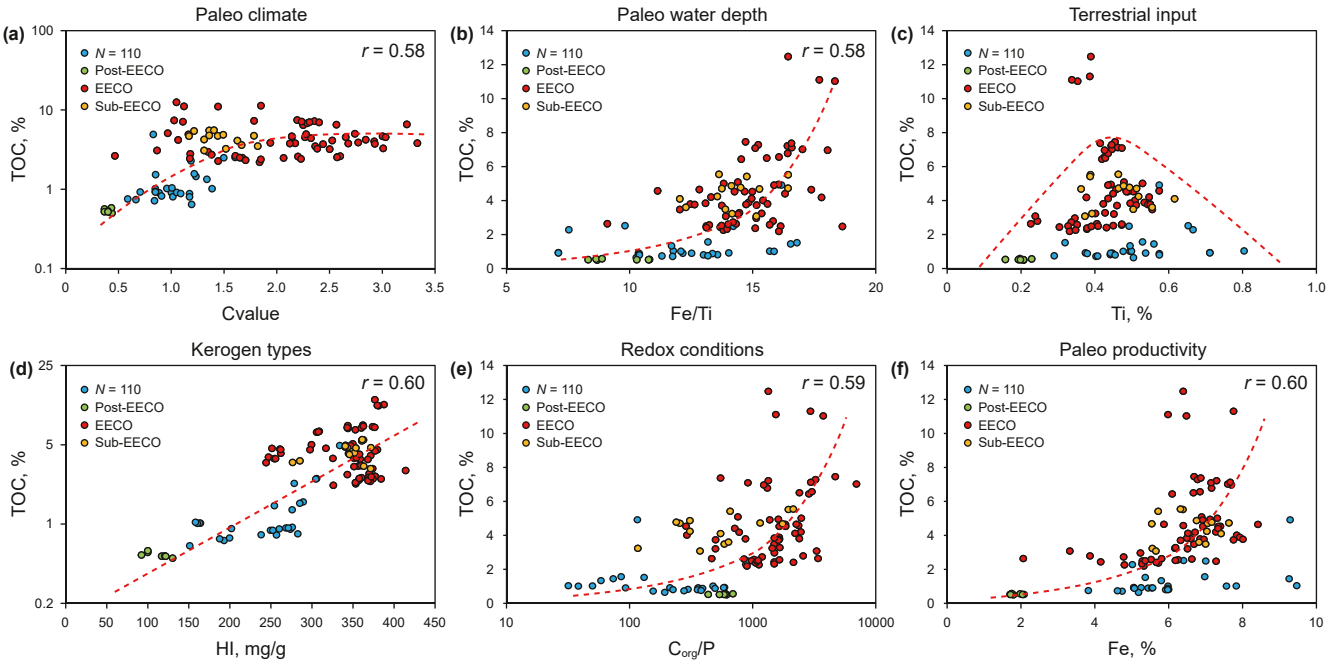

Fig. 9. Controlling factors analysis of OM enrichment. **(a)**paleo climate vs. TOC. **(b)** paleo water depth vs. TOC. **(c)** terrestrial input vs. TOC. **(d)** kerogen types vs. TOC. **(e)** redox conditions vs. TOC. **(f)** paleo productivity vs. TOC. Dots of yellow, red, and green represent the samples before (Sub-EECO), during (EECO), and after the EECO (Post-EECO), respectively. Blue dots represent the other samples besides Sub-EECO, EECO, and Post-EECO. The red lines and "*r*" represent the trends and correlations of TOC with changes in ancient environments, respectively.

OM enrichment. During the EECO, increased paleo productivity, reflected by elevated Fe contents, accelerated OM accumulation of the lake (Fig. 9(f)).

To quantitatively assess the key factors controlling OM enrichment, we removed extreme outliers from the original 110 datasets using Z-scores, resulting in a refined dataset of 97 samples for Pearson correlation analysis (Fig. 10). Given the nonlinear relationship between TOC and terrestrial input (Fig. 9(c)), terrestrial input was excluded as a factor influencing TOC content in the correlation analysis. The Pearson correlation results show that TOC content is strongly correlated with OM source and paleo productivity, each with a correlation coefficient of 0.60 (Fig. 10). Notably, the correlation between terrestrial input and paleo productivity is 0.79, confirming that terrestrial input is a key nutrients sources in the lake (Fig. 10). The correlation between terrestrial input and redox conditions is weak ($r = -0.02$), suggesting that the impact of terrestrial input on OM enrichment outweighs any dilution effects. The Pearson correlation coefficients for TOC with redox conditions, paleoclimate, and paleo water depth are 0.59, 0.58, and 0.58, respectively (Fig. 10). This indicates that OM enrichment and preservation occur under warm, humid climates, anoxia water conditions, and high productivity lakes environments (Fig. 7(e), 8(e) and 8(f)). The lower Mbr. WC Fm., deposited in freshwater environments, shows minimal impact from paleo salinity fluctuations on TOC content (r=0.04). Additionally, the correlation coefficients for OM types with paleo water depth (0.65), paleo productivity with paleoclimate (0.66), and paleo productivity with paleo water depth (0.61) all exceed 0.6, indicating that changes in paleoclimate and paleo water depth during the EECO had a positive feedback mechanism on OM sources and paleo productivity.

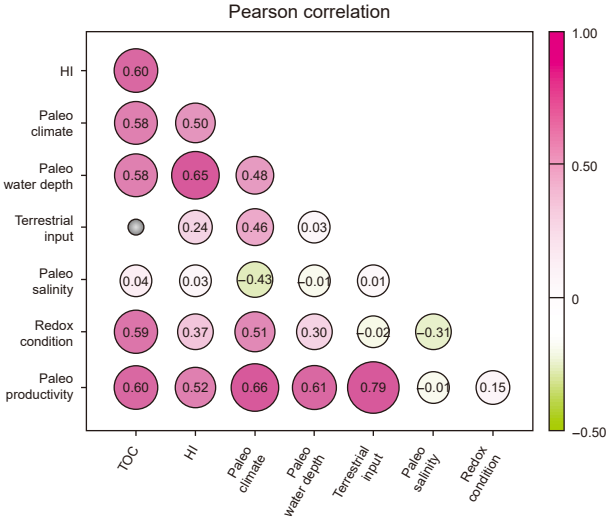

Fig. 10. The Pearson correlation coefficient analysis illustrates the correlations among TOC, HI, paleoclimate, paleo water depth, terrestrial input, paleo salinity, redox conditions, and productivity in the Kaiping Sag, with the numerical values representing the correlation coefficients (r). Pink cycles indicate positive correlations, while green cycles indicate negative correlations. The size and brightness of the circles reflect the strength of the correlations: larger and more vibrant circles indicate stronger relationships among the variables. No Pearson correlation analysis was performed between TOC and terrestrial input.

5.4.2. EECO drove the OM enrichment

The EECO represents the peak of the early Paleogene greenhouse climate (Bornemann et al., 2016). Paleotemperature during this period was approximately 2.6–8.9 °C higher than present (Li et al., 2022) and elevated sea surface temperature around 37 °C across the entire succession (Schaefer et al., 2022). The duration and intensity of environmental response during the EECO were the most extreme since the Eocene, leading to the continuous deposition of 200-m-thick organic-rich mudstone, with TOC exceeding 4.0% and type I kerogen (Fig. 9). Notable examples include the oil shale of the Green River Formation in the Green River Basin

(Bradley et al., 1969; Hyland et al., 2013), the black carbonaceous mudstones of the Guchengzi Fm. in the Fushun Basin (Li et al., 2022a, 2022b), the organic-rich mudstones of the Liushagang Fm. in the Beibuwan Basin (Wei et al., 2023), and the shales of the Shahejie Fm in the Bohai Bay Basin (Wu et al., 2023), all of which were deposited during the EECO.

Before the EECO event, the Kaiping Sag underwent a pre-warming stage marked by climate changes similar to those of the EECO, though with weaker environmental response and shorter duration. As a result, the mudstones deposited during this period were thinner and less organic-rich than those deposited during the EECO.

The environmental response during the EECO is thought to have primarily controlled OM enrichment by influencing paleo productivity and preservation conditions in the lakes. Temperature rises during the EECO are believed to be closely linked to rapid increases in atmospheric CO_2 levels (Royer et al., 2001; Hyland and Sheldon, 2013; Cui and Schubert, 2016; Hyland et al., 2018). The rapid eruption of the Linzizong volcanic rocks across the Tibetan Plateau and potentially extending into Southeast Asia released

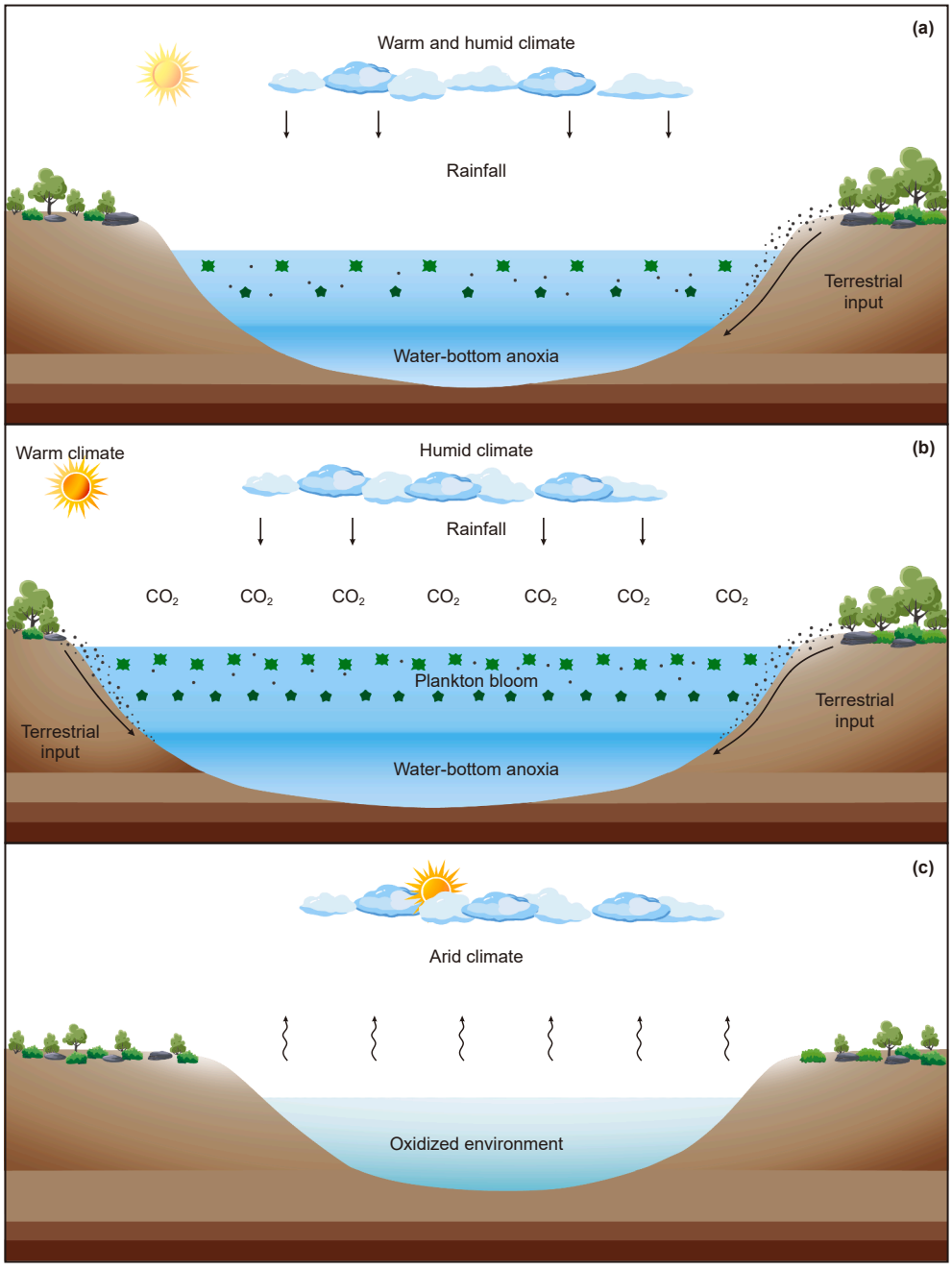

Fig. 11. OM enrichment models during the EECO. **(a)** Before the EECO, the Early Eocene Wenchang Formation recorded a pre-warming event characterized by climate changes similar to the EECO, but with a lower degree of environmental response and shorter duration. **(b)** During the EECO, the lake environment experienced a warm and humid climate, high lake level, high terrestrial input, anoxia conditions, and elevated productivity, ultimately reflected in increased OM burial and high TOC. **(c)** The climate changes and environmental responses after the EECO were opposite to those during the EECO, ultimately resulting in nutrient depletion in the lakes.

amounts of CO_2, which may have driven the EECO (Zhang et al., 2022b, 2023). Although the role of CO_2 may vary across oceanic, mid-to high-latitude, and low latitude regions, the overall rise in global atmospheric pCO_2 levels during the EECO is clear. We focus here on the commonalities associated with this increase. *Pediastrum*, a type of planktonic algae, is the primary OM source for the organic-rich mudstones in the Kaiping Sag (Xiong et al., 2021; He et al., 2024) and its highly sensitive to atmospheric CO_2 levels. As pCO_2 increased, the rate of algal photosynthesis was enhanced, leading to elevated organic productivity within the lake systems during the EECO (Fig. 11(b), Falkowski, 2012). This increase in productivity is synchronous with the most significant biological changes observed in the southwestern Pacific, including increased diversity of calcareous nannofossils, the highest abundance of warm-water taxa and planktic foraminifera, and a long-term shift toward more abundant and diverse angiosperm vegetation (Crouch et al., 2020). Furthermore, Tanaka et al. (2022) reported early Eocene marine Os isotope records of thermal events at Ocean Drilling Program Site 752 in the southern Indian Ocean, showing that continental silicate weathering intensified during this period (Yarincik et al., 2000; Tanaka et al., 2022). The intensified weathering contributed to higher terrestrial input into lakes (Fig. 11(b)). On one hand, weathering of nutrients-rich proximal source areas promoted lake productivity. On the other hand, increased continental runoff and terrestrial inputs led to stratified water columns and bottom-water anoxia (Li et al., 2016; Liu et al., 2024b), providing favorable conditions for OM preservation (Fig. 11(b)). Moreover, elevated lake levels resulted in the stagnation of bottom waters, creating abundant habitats for algae and facilitating the formation and preservation of OM (e.g., Sames et al., 2020; Liu et al., 2024b). Hence, the warm climate and elevated pCO_2 were key factors contributing to the high quality of lacustrine source rocks in the Kaiping Sag during the EECO.

The post-EECO cooling is often attributed to a decline in atmospheric pCO_2 levels (Fig. 11(c), Pearson and Palmer, 2000; Demicco et al., 2003; Pagani et al., 2005; Zachos et al., 2008; Bornemann et al., 2016). During this period, the environmental response in the Kaiping Sag was the opposite of that during the EECO, leading to nutrient depletion in the lake and almost no deposition of organic-rich rocks.

6. Conclusions

At approximately 52.5–52 Ma (Sub-EECO) and 51.5–48.7 Ma (EECO), the lower Mbr. WC Fm. recorded two intervals of sustained warming, marked by fluctuations in climate indicators and the deposition of organic-rich mudstone. This evidence suggests that the Wenchang formation experienced warming before the EECO, underscoring the sensitivity of terrestrial records.

During the EECO, the Kaiping Sag experienced a warm and humid climate, high lake levels, increased terrestrial input, anoxia conditions, and elevated productivity. While the environmental responses during the sub-EECO were similar to those of the EECO, there were of lower intensity and shorter duration. In contrast, the post-EECO period exhibited climatic and environmental responses opposite to those of the EECO.

The EECO event drove OM enrichment by influencing the lake paleo-productivity and preservation conditions. The global increase in productivity was synchronized, driven by rising atmospheric pCO_2 levels that enhanced algal photosynthesis. Increased terrestrial inputs and elevated lake levels caused the stagnation of bottom waters, creating favorable conditions for OM formation and preservation.

CRediT authorship contribution statement

Jing Guo: Data curation, Writing – original draft, Conceptualization. **Guang-Rong Peng:** Project administration, Validation. **Fu-Jie Jiang:** Supervision, Writing – review & editing. **Yu-Qi Wu:** Validation, Software. **Hong-Bo Li:** Project administration. **Ya-Qi Li:** Data curation. **Xin-Wei Qiu:** Validation. **Jun-Jie Cai:** Formal analysis. **Fu-Sheng Yu:** Funding acquisition. **Xin Chen:** Visualization. **Biao Jiang:** Methodology. **Li-Shan Tang:** Visualization.

Declaration of competing interest

The authors declare that they have no known competing financial interests or personal relationships that could have appeared to influence the work reported in this paper.

Acknowledgments

This research was funded by the National Natural Science Foundation of China (42372147). The authors thank the State Key Laboratory of Petroleum Resources and Engineering, China University of Petroleum (Beijing) for their support of this research.

Appendix A. Supplementary data

Supplementary data to this article can be found online at https://doi.org/10.1016/j.petsci.2025.08.005.

References

Abels, H., Hilgen, F., Krijgsman, W., et al., 2005. Long period orbital control on middle Miocene global cooling: integrated stratigraphy and astronomical tuning of the blue clay formation on Malta. Paleoceanography 20 (4), PA001129. https://doi.org/10.1029/2004PA001129.

Agnini, C., Fornaciari, E., Raffi, I., et al., 2014. Biozonation and biochronology of Paleogene calcareous nannofossils from low and middle latitudes. Newsl. Stratigr. 47, 131–181. https://doi.org/10.1127/0078-0421/2014/0042.

Algeo, T.J., Li, C., 2020. Redox classification and calibration of redox thresholds in sedimentary systems. Geochem. Cosmochim. Acta 287, 8–26. https://doi.org/10.1016/j.gca.2020.01.055.

Algeo, T.J., Tribovillard, N., 2009. Environmental analysis of paleoceanographic systems based on molybdenum–uranium covariation. Chem. Geol. 268 (3–4), 211–225. https://doi.org/10.1016/j.chemgeo.2009.09.001.

Algeo, T.J., Ingall, E., 2007. Sedimentary c_{org}: p ratios, paleocean ventilation, and Phanerozoic atmospheric pO_2. Palaeogeogr. Palaeoclimatol. Palaeoecol. 256 (3–4), 130–155. https://doi.org/10.1016/J.PALAEO.2007.02.029.

Algeo, T.J., Lyons, T.W., 2006. Mo-total organic carbon covariation in modern anoxic marine environments: implications for analysis of paleoredox and paleohydrographic conditions. Paleoceanography 21, 1–23. https://doi.org/10.1029/2004PA001112.

Algeo, T.J., Scheckler, S.E., 1998. Terrestrial-marine teleconnections in the Devonian: links between the evolution of land plants, weathering processes, and marine anoxic events. Phil. Trans. R. Soc. Lond. B353, 113–130. https://doi.org/10.1098/rstb.1998.0195.

Anagnostou, E., John, E.H., Edgar, K.M., et al., 2016. Changing atmospheric CO_2 concentration was the primary driver of early Cenozoic climate. Nature 533, 380–384. https://doi.org/10.1038/nature17423.

Bijl, P.K., Houben, A.J.P., Schouten, S., et al., 2010. Transient middle Eocene atmospheric CO_2 and temperature variations. Science 330, 819–821. https://doi.org/10.1126/science.1193654.

Bornemann, A., D'haenens, S., Norris, R.D., et al., 2016. The demise of the early Eocene greenhouse – decoupled deep and surface water cooling in the eastern North Atlantic. Glob. Planet. Chang. 145, 130–140. https://doi.org/10.1016/j.gloplacha.2016.08.010.

Bornemann, A., Norris, R.D., Lyman, J.A., et al., 2014. Persistent environmental change after the Paleocene–Eocene Thermal Maximum in the eastern North Atlantic. Earth Planet Sci. Lett. 394, 70–81. https://doi.org/10.1016/j.epsl.2014.03.017.

Bosmans, J.H.C., Hilgen, F.J., Tuenter, E., 2015. Obliquity forcing of low-latitude climate. Clim. Past. 11, 1335–1346. https://doi.org/10.5194/cp-11-1335-2015.

Boulila, S., 2019. Coupling between grand cycles and events in Earth's climate during the past 115 million years. Sci. Rep. 9, 327. https://doi.org/10.1038/s41598-018-36509-7.

Boulila, S., Galbrun, B., Miller, K.G., et al., 2011. On the origin of Cenozoic and Mesozoic "third-order" eustatic sequences. Earth Sci. Rev. 109, 94–112. https://doi.org/10.1016/j.earscirev.2011.09.003.
Boulila, S., Vahlenkamp, M., De Vleeschouwer, D., et al., 2018. Towards a robust and consistent middle Eocene astronomical timescale. Earth Planet Sci. Lett. 486, 94–107. https://doi.org/10.1016/j.epsl.2018.01.003.
Cai, S., Peng, G.R., Chen, Z.M., et al., 2023. Paleogene tectonic evolution of Kaiping Sag, pearl river mouth basin. Marine geol. Quat. Geology 43 (2), 106–118. https://doi.org/10.16562/j.cnki.0256-1492.2022072702 (in Chinese).
Calvert, S.E., Pedersen, T.F., 2007. Chapter fourteen elemental proxies for palaeoclimatic and palaeoceanographic variability in marine sediments: Interpretation and application. Dev. Mar. Geol. 1, 567–644. https://doi.org/10.1016/S1572-5480(07)01019-6.
Cleveland, W.S., 1979. Robust locally weighted regression and smoothing scatterplots. J. Am. Stat. Assoc. 74, 829–836. https://doi.org/10.1080/01621459.1979.10481038.
Cramer, B.S., Wright, J.D., Kent, D.V., et al., 2003. Orbital climate forcing of $\delta^{13}C$ excursions in the late Paleocene-early Eocene (chrons C24n–C25n). Paleoceanography 18 (4), 1097. https://doi.org/10.1029/2003PA000909.
Cramwinckel, M.J., Huber, M., Kocken, I.J., et al., 2018. Synchronous tropical and polar temperature evolution in the Eocene. Nature 559 (7714), 382–386. https://doi.org/10.1038/s41586-018-0272-2.
Crouch, E.M., Shepherd, C.L., Morgans, H.E.G., et al., 2020. Climatic and environmental changes across the early Eocene climatic optimum at mid-Waipara river, Canterbury basin, New Zealand. Earth Sci. Rev. 200, 102961. https://doi.org/10.1016/j.earscirev.2019.102961.
Cui, Q.Y., Zhao, Y., 2019. Climatic abrupt events implied by lacustrine sediments of aran Crater Lake, in the central great khingan Mountains, NE China during Holocene. Quat. Sci. 39 (6), 1346–1356. https://doi.org/10.11928/j.issn.1001-7410.2019.06.03 (in Chinese).
Cui, Y., Schubert, B.A., 2016. Quantifying uncertainty of past pCO_2 determined fromhanges in C_3 plant carbon isotope fractionation. Geochem. Cosmochim. Acta 172, 27–138. https://doi.org/10.1016/j.gca.2015.09.032.
Cui, Y., Schubert, B.A., 2018. Towards determination of the source and magnitude of atmospheric pCO_2 change across the early Paleogene hyperthermals. Glob. Planet. Chang. 170, 120–125. https://doi.org/10.1016/j.gloplacha.2018.08.011.
DeConto, R., Galeotti, S., Pagani, M., et al., 2012. Past extreme warming events linked to massive carbon release from thawing permafrost. Nature 484, 87–91. https://doi.org/10.1038/nature10929.
Demaison, G.J., Moore, G.T., 1980. Anoxic environments and oil source bed genesis. Org. Geochem. 2 (1), 9–31. https://doi.org/10.1016/0146-6380(80)90017-0.
Demicco, R.V., Lowenstein, T.K., Hardie, L.A., 2003. Atmospheric pCO_2 since 60 Ma from records of seawater pH, calcium, and primary carbonate mineralogy. Geology 31, 793–796. https://doi.org/10.1130/G19727.1.
Dickens, G.R., 2011. Down the rabbit hole: toward appropriate discussion of methane release from gas hydrate systems during the Paleocene-Eocene thermal maximum and other past hyperthermal events. Clim. Past 7, 831–846. https://doi.org/10.5194/cp-7-831-2011.
Dinare`s-Turell, J., Martinez-Braceras, N., Payros, A., 2018. High-resolution integrated cyclostratigraphy from the Oyambre Section (Cantabria, N Iberian Peninsula): Constraints for orbital tuning and correlation of middle Eocene Atlantic deep-sea records. G-cubed 19, 787–806. https://doi.org/10.1002/2017gc007367.
Doney, S.C., Fabry, V.J., Feely, R.A., et al., 2009. Ocean acidification: the other CO_2 problem. Ann. Rev. Mar. Sci. 1, 169–192. https://doi.org/10.1146/annurev.marine.010908.163834.
Dong, H.L., Zeng, Q., Sheng, Y.Z., et al., 2023. Coupled iron cycling and organic matter transformation across redox interfaces. Nat. Rev. 4, 659–673. https://doi.org/10.1038/s43017-023-00470-5.
Dzombak, R.M., Sheldon, N.D., 2022. Terrestrial records of weathering indicate three billion years of dynamic equilibrium. Gondwana Res. 109, 376–393. https://doi.org/10.1016/j.gr.2022.05.009.
Falkowski, P., 2012. Ocean Science: the power of plankton. Nature 483, S17–S20. https://doi.org/10.1038/483S17a.
Fan, X.J., Wang, C.L., Teng, X.H., 2024. Mechanisms of terrestrial organic matter accumulation across the Paleocene-Eocene thermal maximum in the Jianghan Basin, Central China. Palaeogeogr. Palaeoclimatol. Palaeoecol. 684, 112283. https://doi.org/10.1016/j.palaeo.2024.112283.
Gao, Y.D., Liu, J., Peng, G.R., et al., 2024a. New fields and resource potential of oil and gas exploration in Pearl River Mouth Basin. Acta Petrol. Sin. 45 (1), 183–201. https://doi.org/10.7623/syxb202401011 (in Chinese).
Gao, Y.D., Peng, G.R., Chen, Z.M., et al., 2023. Breakthrough and significance of deep-water Paleogene exploration in Kaiping sag, Pearl River Mouth Basin. Acta Pet. Sin. 44 (7), 1029–1040. https://doi.org/10.7623/syxb202307001 (in Chinese).
Gao, Y., Long, Z., Chen, C., et al., 2024b. Geochemical characteristics and genesis of middle and deep oil in Southern Region of kaiping Sag, Pearl River mouth Basin. J. Jilin Univ. Earth Sci. Ed. 54 (6), 1883–1895. https://doi.org/10.13278/j.cnki.jjuese.20240248 (in Chinese).
Garcia-Soto, C., Cheng, L., Caesar, L., et al., 2021. An overview of ocean climate change indicators: sea surface temperature, ocean heat content, ocean pH, dissolved oxygen concentration, Arctic sea ice extent, thickness and volume, sea level and strength of the AMOC (Atlantic Meridional Overturning Circulation). Front. Mar. Sci. 8. https://doi.org/10.3389/fmars.2021.642372.
Gobler, C.J., 2020. Climate change and harmful algal blooms: Insights and perspective. Harmful Algae 91, 101731. https://doi.org/10.1016/j.hal.2019.101731.
Guo, X.C., He, S., 2007. Source rock thermal and maturity history modeling in the Baiyun Sag of the Pearl River Mouth Basin. Pet. Geol. Exp. 29 (4), 420–425. https://doi.org/10.11781/sysydz200704420 (in Chinese).
Guo, W., Zhang, W.G., Li, Y.H., et al., 2020. Geochemistry of 7 Member shale of the Dameigou Formation in the Northern Qaidam Basin, China: significance and implication for provenance and source weathering in the late Middle Jurassic. Acta Sedimentol. Sin. 38 (3), 676–686. https://doi.org/10.14027/j.issn.1000-0550.2019.103 (in Chinese).
Guo, X.Y., Zhang, H.L., Li, L., et al., 2020. Biomarker records of phytoplankton productivity and community structure changes in the mud area of the Yangtze River Estuary in the East China Sea during the last 30 years. Periodical Ocean Univ. China 50 (2), 85–94. https://doi.org/10.16441/j.cnki.hdxb.20190164 (in Chinese).
He, Z.T., Yin, X.D., Chen, S.J., et al., 2024. Origin of the abnormal carbon isotopic in organic matter of the Wenchang Formation, Zhu III sub-basin, Pearl River Mouth. Acta Geol. Sin. 98 (1), 266–279. https://doi.org/10.19762/j.cnki.dizhixuebao.2023038 (in Chinese).
Hao, Y., Xu, Y., Xu, S., 1996. Tertiary Micropaleontology and Paleoceanography in the Pearl River Mouth Basin, South China Sea. China University of Geosciences Press, Wuhan (in Chinese).
Hollis, C.J., Taylor, K.W.R., Handley, L., et al., 2012. Early Paleogene temperature history of the Southwest Pacific Ocean: Reconciling proxies and models. Earth Planet Sci. Lett. 349–350, 53–66. https://doi.org/10.1016/j.epsl.2012.06.024.
Horton, R., Herweijer, C., Rosenzweig, C., Liu, J., Gornitz, V., Ruane, A.C., 2008. Sea level rise projections for current generation CGCMs based on the semi-empirical method. Geophys. Res. Lett. 35 (2). https://doi.org/10.1029/2007GL032486.
Hu, J.J., Ma, Y.S., Wang, Z.X., et al., 2017. Palaeoenvironment and palaeoclimate of the Middle to late Jurassic revealed by geochemical records in northern margin of Qaidam Basin. J. Palaeogeogr. 19 (3), 480–490. https://doi.org/10.7605/gdlxb.2017.03.037 (in Chinese).
Hu, T., Pang, X.Q., Jiang, F.J., et al., 2021. Factors controlling differential enrichment of organic matter in saline lacustrine rift basin: A case study of third member Shahejie Fm. in Dongpu Depression. Acta Sedimentol. Sin. 39 (1), 140–152. https://doi.org/10.14027/j.issn.1000-0550.2020.125 (in Chinese).
Hu, Y., 2013. The geological application of XRF element well logging technique in Sichuan Basin. Sino-Global Energy 18 (11), 58–62. https://doi.org/10.3969/j.issn.1673-579X.2013.11.012 (in Chinese).
Hu, Z.C., Gao, S., 2008. Upper crustal abundances of trace elements: A revision and update. Chem. Geol. 253 (3–4), 205–221. https://doi.org/10.1016/j.chemgeo.2008.05.010.
Huang, L.S., Zhong, B.Z., 1998. New materials of the calcareous nannofossil in the middle Eocene Wenchang Formation from the Pearl River Mouth Basin. China Offshore Oil Gas Geol. 12 (1), 31–35.
Huang, L.S., 1999. Tertiary biostratigraphic framework of Pearl River Mouth Basin. China Offshore Oil Gas Geol. 13 (6), 406–415.
Huang, C.J., 2014. The current status of cyelostratigraphy and astrochronology in the Mesozoie. Earth Sci. Front. 21 (2), 48–66. https://doi.org/10.13745/jesf.2014.02.005.
Huang, R.D., Jiang, F.J., Chen, D., et al., 2023a. Astrochronology and carbon-isotope stratigraphy of the Fengcheng Formation, Junggar Basin: Terrestrial evidence for the Carboniferous-Permian Boundary. Gondwana Res. 116, 1–11. https://doi.org/10.1016/j.gr.2022.12.016.
Huang, X., Chen, W.T., Wang, W.Y., et al., 2023b. Sequence stratigraphy and sedimentary filling characteristics of Wenchang Formation under the background of tectonic transformation in the northern Xiang Depression of the Pearl River Mouth Basin. Mar. Geology Front. 39 (5), 43–54. https://doi.org/10.16028/j.1009-2722.2022.179.
Hyland, E.G., Huntington, K.W., Sheldon, N.D., et al., 2018. Temperature seasonality in the North American continental interior during the early Eocene climatic optimum. Clim. Past Discuss 1–39. https://doi.org/10.5194/cp-14-1391-2018.
Hyland, E.G., Sheldon, N.D., 2013. Coupled CO_2-climate response during the Early Eocene Climatic Optimum. Palaeogeogr. Palaeoclimatol. Palaeoecol. 369, 125–135. https://doi.org/10.1016/j.palaeo.2012.10.011.
Ingall, E., Jahnke, R., 1997. Influence of water-column anoxia on the elemental fractionation of carbon and phosphorus during sediment diagenesis. Mar. Geol. 139 (1–4), 219–229. https://doi.org/10.1016/S0025-3227(96)00112-0.
Jones, B., Manning, D.A.C., 1994. Comparison of geochemical indices used for the interpretation of palaeoredox conditions in ancient mudstones. Chem. Geol. 111 (1–4), 111–129. https://doi.org/10.1016/0009-2541(94)90085-X.
Katz, M.E., Miller, K.G., Wright, J.D., et al., 2008. Stepwise transition from the Eocene greenhouse to the Oligocene icehouse. Nat. Geosci. 1, 329–334. https://doi.org/10.1038/NGEO179.
Kodama, K.P., Hinnov, L.A., 2014. Rock Magnetic Cyclostratigraphy. New Analytical Methods in Earth and Environmental Science Series. Wiley-Blackwell, pp. 1–147. https://doi.org/10.1002/9781118561294.
Laskar, J., Fienga, A., Gastineau, M., et al., 2011. La2010: a new orbital solution for the long-term motion of the Earth. Astron. Astrophys. 532, A89. https://doi.org/10.1051/0004-6361/201116836.
Laskar, J., Robutel, P., Joutel, F., et al., 2004. A long-term numerical solution for the insolation quantities of the Earth. Astron. Astrophys. 428, 261–285. https://doi.org/10.1051/0004-6361:20041335.

Lauretano, V., Kennedy-Asser, A.T., Korasidis, V.A., et al., 2021. Eocene to Oligocene terrestrial Southern Hemisphere cooling caused by declining pCO_2. Nat. Geosci. 14, 659–664. https://doi.org/10.1038/s41561-021-00788-z.

Lauretano, V., Littler, K., Polling, M., et al., 2015. Frequency, magnitude and character of hyperthermal events at the onset of the early Eocene Climatic Optimum. Clim. Past Discuss 11, 1313–1324. https://doi.org/10.5194/cp-11-1313-2015.

Li, B., Zhuang, X., Liu, X., et al., 2016. Mineralogical and geochemical composition of Middle Permian Lucaogou Formation in the southern Junggar Basin, China: Implications for paleoenvironment, provenance, and tectonic setting. Arab. J. Geosci. 9, 1–16. https://doi.org/10.1007/s12517-015-2154-3.

Li, M., Kump, L.R., Hinnov, L.A., Mann, M.E., 2018a. Tracking variable sedimentation rates and astronomical forcing in Phanerozoic paleoclimate proxy series with evolutionary correlation coefficients and hypothesis testing. Earth Planet Sci. Lett. 501, 165–179. https://doi.org/10.1016/j.epsl.2018.08.041.

Li, S.B., Wang, Y.J., Wu, S.M., 2018b. Meso-Cenozoic tectonothermal pattern of the Pearl River Mouth Basin: Constraints from zircon and apatite fission track data. Earth Sci. Front. 25 (1), 95–107. https://doi.org/10.13745/j.esf.yx.2017-5-20.

Li, Y.J., Sun, P.C., Liu, Z.J., et al., 2020. Geochemistry of the Permian oil shale in the northern Bogda Mountain, Junggar Basin, northwest China: implications for weathering, provenance, and tectonic setting. ACS Earth Space Chem. 4 (8), 1332–1348. https://doi.org/10.1021/acsearthspacechem.0c00113.

Li, Y.J., Sun, P.C., Liu, Z.J., et al., 2021. Factors controlling the distribution of oil shale layers in the Eocene Fushun Basin, NE China. Mar. Pet. Geol. 134, 105350. https://doi.org/10.1016/j.marpetgeo.2021.105350.

Li, Y.J., Sun, P.C., Liu, Z.J., et al., 2022a. Eocene hyperthermal events in the terrestrial system: Geochronological and astrochronological constraints in the Fushun Basin, NE China. Mar. Pet. Geol., 105604 https://doi.org/10.1016/j.marpetgeo.2022.105604.

Li, Y.J., Sun, P.C., Liu, Z.J., et al., 2022b. Quantitative reconstruction of atmospheric pCO_2 sources during Eocene hyperthermal events based on data from the Fushun Basin, Northeast China. Palaeogeogr. Palaeoclimatol. Palaeoecol. 601, 111099. https://doi.org/10.1016/j.palaeo.2022.111099.

Liang, Y., 2007. Fundamentals of X-ray Fluorescence Spectroscopy. Science Press, Beijing.

Liu, J., Shi, J.Y., Lu, Y.C., et al., 2024b. Astronomical forcing of terrestrial organic carbon burial in East Asia during the Eocene. Earth Planet Sci. Lett. 646, 119014. https://doi.org/10.1016/j.epsl.2024.119014.

Liu, P., Tan, X.F., Chen, Q., 2017. Water redox conditions and environment for source rock deposition in lacustrine during the Initial Eocene Thermal Maximum (IETM): A case study on the Paleogene Kongdian Formation in the Dongying Sag. Oil Gas Geol. 38 (1), 39–48. https://doi.org/10.11743/ogg20170105.

Liu, W., Gao, P., Xiao, X.M., 2024a. Variable depositional environments and organic matter enrichment of early Cambrian shales in the Middle Yangtze region, South China. J. Asian Earth Sci. 259, 105874. https://doi.org/10.1016/j.jseaes.2023.105874.

Lourens, L.J., Sluijs, A., Kroon, D., et al., 2005. Astronomical pacing of late Palaeocene to early Eocene global warming events. Nature 435 (7045), 1083–1087. https://doi.org/10.1038/nature03814.

Lunt, D.J., Jones, T.D., Heinemann, M., et al., 2012. A model-data comparison for a multi-model ensemble of early Eocene atmosphere-ocean simulations: EoMIP. Clim. Past 8 (5), 1717. https://doi.org/10.5194/cp-8-1717-2012.

Ma, B.S., 2020. The Cenozoic Structural Characteristics and Tectonic Evolution of the Pearl River Mouth Basin, Northern South China Sea. China University of Petroleum, Beijing (in Chinese). https://doi.org/10.27643/d.cnki.gsybu.2020.000064.

Mann, M.E., Lees, J.M., 1996. Robust estimation of background noise and signal detection in climatic time series. Clim. Change 33, 409–445. https://doi.org/10.1007/BF00142586.

Marshall, M.H., Lamb, H.F., Huws, D., et al., 2011. Late Pleistocene and Holocene drought events at Lake Tana, the source of the Blue Nile. Glob. Planet. Chang. 78, 147–161. https://doi.org/10.1016/j.gloplacha.2011.06.004.

McInerney, F.A., Wing, S.L., 2011. The Paleocene-Eocene Thermal Maximum: A perturbation of carbon cycle, climate, and biosphere with implications for the future. Annu. Rev. Earth Planet Sci. 39, 489–516. https://doi.org/10.1146/annurev-earth-040610-133431.

Meijer, N., Licht, A., Woutersen, A., et al., 2024. Proto-monsoon rainfall and greening in Central Asia due to extreme early Eocene warmth. Nat. Geosci. 17, 158–164. https://doi.org/10.1038/s41561-023-01371-4.

Meyers, S.R., 2015. The evaluation of eccentricity-related amplitude modulation and bundling in paleoclimate data: An inverse approach for astrochronologic testing and time scale optimization. Paleoceanography 30, 1625–1640. https://doi.org/10.1002/2015PA002850.

Mishra, P., Pandey, C.M., Singh, U., et al., 2019. Descriptive statistics and normality tests for statistical data. Ann. Card Anaesth. 22 (1), 67–72. https://doi.org/10.4103/aca.ACA_157_18.

Mitchell, R.N., Bice, D.M., Montanari, A., et al., 2008. Oceanic anoxic cycles? Orbital prelude to the Bonarelli Level (OAE 2). Earth Planet Sci. Lett. 267 (1), 1–16. https://doi.org/10.1016/j.epsl.2007.11.026.

Moradi, A.V., Sarı, A., Akkaya, P., 2016. Geochemistry of the Miocene oil shale (Hançili formation) in the Çankırı-Çorum basin, Central Turkey: Implications for paleoclimate conditions, source-area weathering, provenance and tectonic setting. Sediment. Geol. 341, 289–303. https://doi.org/10.1016/j.sedgeo.2016.05.002.

Morford, J.L., Emerson, S., 1999. The geochemistry of redox sensitive trace metals in sediments. Geochem. Cosmochim. Acta 63, 1735–1750. https://doi.org/10.1016/S0016-7037(99)00126-X.

Murphy, A.E., Sageman, B.B., Hollader, D.J., et al., 2000. Black shale deposition and faunal overturn the Devonian Appalachian Basin: Clastic starvation, seasonal water-column mixing, and efficient biolimiting nutrient recycling. Paleoceanography 15 (3), 280–291. https://doi.org/10.1029/1999PA000445.

Nie, G.Q., He, D.F., Li, X.P., et al., 2021. Tectonic subsidence and its main controlling factors of Kaiping Sag in Pearl River Mouth Basin. Mar. Origin Pet. Geology 26 (3), 253–262. https://doi.org/10.3969/j.issn.1672-9854.2021.03.007.

Olsen, P.E., Kent, D.V., Whiteside, J.H., 2011. Implications of the Newark Supergroup-based astrochronology and geomagnetic polarity time scale (Newark-APTS) for the tempo and mode of the early diversification of the Dinosauria. Earth Env. Sci. T. R. So. 101 (3), 201. https://doi.org/10.7916/D87W6NT2.

Pagani, M., Zachos, J.C., Freeman, K.H., et al., 2005. Marked decline in atmospheric carbon dioxide concentrations during the Paleogene. Science 309, 600–603. https://doi.org/10.1126/science.1110063.

Parrish, J.T., 1995. Paleogeography of C_{org}-rich Rocks and the Preservation Versus Production Controversy. AAPG Tulsa, pp. 1–20. https://doi.org/10.1306/St40595C1.

Pearson, P.N., Palmer, M.R., 2000. Atmospheric carbon dioxide concentrations over the past 60 million years. Nature 406, 695–699. https://doi.org/10.1038/35021000.

Peng, G.R., Guo, J., Jiang, F.J., et al., 2023. Geochemicatics characteristics of source rocks and oil source correlation in Kaiping sag, Pearl River Mouth Basin. Acta Petrol. Sin. 44 (10), 1624–1636. https://doi.org/10.7623/syxb202310004 (in Chinese).

Piedrahita, V.A., Roberts, A.P., Rohling, E.J., et al., 2024. Dry hydroclimates in the late Palaeocene-early Eocene hothouse world. Nat. Commun. 15, 7042. https://doi.org/10.1038/s41467-024-51430-6.

Pommer, M., Sarg, J.F., McFarlin, F., 2023. Environmental and microbial influence on chemistry and dolomite formation in an ancient lake, Green River Formation (Eocene), Uinta Basin, Utah. USA J. Sediment. Res. 93 (4), 213–242. https://doi.org/10.2110/jsr.2022.016.

Potter, M.C., Lessing, J.L., Aboufadel, E.F., 2019. Advanced Engineering Mathematics, fourth ed. Springer. https://doi.org/10.1007/978-3-030-17068-4.

Pound, M., Salzmann, U., 2017. Heterogeneity in global vegetation and terrestrial climate change during the late Eocene to early Oligocene transition. Sci. Rep. 7, 43386. https://doi.org/10.1038/srep43386.

Qin, G.Q., 2000. Investigation to the stratigraphy and construction of the comprehensive geologic columnar section of Cenozoic formation in Pearl River Mouth Basin. China Offshore Oil Gas Geol. 14 (1), 21–28.

Rahmstorf, S., 2007. A semi-empirical approach to projecting future sea-level rise. Science 315 (5810), 368–370. https://doi.org/10.1126/science.1135456.

Reagan, M.K., McClelland, W.C., Girard, G., et al., 2013. The geology of the southern Mariana fore-arc crust: Implications for the scale of Eocene volcanism in the western Pacific. Earth Planet Sci. Lett. 380, 41–51. https://doi.org/10.1016/j.epsl.2013.08.013.

Redfield, A.C., 1960. The biological control of chemical factors in the environment. Sci. Prog. 11, 150–170. https://doi.org/10.1086/646891.

Roy, D.K., Roser, B.P., 2013. Climatic control on the composition of Carboniferous Permian Gondwana sediments, Khalaspir Basin, Bangladesh. Gondwana Res. 23 (3), 1163–1171. https://doi.org/10.1016/j.gr.2012.07.006.

Royer, D.L., Wing, S.L., Beerling, et al., 2001. Paleobotanical evidence for near present-day levels of atmospheric CO_2 during part of the Tertiary. Science 292, 2310–2313. https://doi.org/10.1126/science.292.5525.231.

Sames, B., Wagreich, M., Conrad, C.P., Iqbal, S., 2020. Aquifer-eustasy as the main driver of short-term sea-level fluctuations during Cretaceous hothouse climate phases. Geol. Soc. Lond. Spec. Publ. 498, 9–38. https://doi.org/10.1144/SP498-2019-105.

Schaefer, B., Schwark, L., Böttcher, M.E., 2022. Paleoenvironmental evolution during the Early Eocene Climate Optimum in the Chicxulub impact crater. Earth Planet Sci. Lett. 589, 117589. https://doi.org/10.1016/j.epsl.2022.117589.

Schenau, S.J., Reichart, G.J., De Lange, G.J., 2005. Phosphorus burial as a function of paleoproductivity and redox conditions in Arabian Sea sediments. Geochem. Cosmochim. Acta 69 (4), 919–931. https://doi.org/10.1016/j.gca.2004.05.044.

Scotese, C., 2014. Atlas of Paleogene Paleogeographic Maps (Mollweide Projection), Maps 8–15, Volume 1, the Cenozoic, PALEOMAP Atlas for Arcgis. PALEOMAP Project, Evanston, IL. https://doi.org/10.13140/2.1.3417.6961.

Shao, L., Meng, A.H., Li, Q.Y., 2017. Detrital zircon ages and elemental characteristics of the Eocene sequence in IODP Hole U1435A: Implications for rifting and environmental changes before the opening of the South China Sea. Mar. Geology 394, 39–51. https://doi.org/10.1016/j.margeo.2017.08.002.

Shi, H.S., Du, S.Y., Zhu, J.Y., et al., 2017. Petroleum Geology of Paleogene in the Pearl River Mouth Basin. Geology Press, Beijing.

Shi, H.S., Du, J.Y., Mei, L.F., 2020. Huizhou Movement and its significance in Pearl River Mouth Basin, China. Pet. Explor. Dev. 47 (3), 447–461. https://doi.org/10.11698/PED.2020.03.02.

Shi, J., Jin, Z., Liu, Q., et al., 2019. Cyclostratigraphy and astronomical tuning of the middle Eocene terrestrial successions in the Bohai Bay Basin, Eastern China. Glob. Planet. Chang. 174, 115–126. https://doi.org/10.1016/j.gloplacha.2019.01.001.

Shi, J., Jin, Z., Liu, Q., et al., 2020. Depositional process and astronomical forcing model of lacustrine fine-grained sedimentary rocks: A case study of the early

Paleogene in the Dongying Sag, Bohai Bay Basin. Mar. Pet. Geol. 113, 103995. https://doi.org/10.1016/j.marpetgeo.2019.08.023.
Shi, J., Jin, Z., Liu, Q., et al., 2021. Sunspot cycles recorded in Eocene lacustrine fine-grained sedimentary rocks in the Bohai Bay Basin, Eastern China. Glob. Planet. Chang. 205, 103614. https://doi.org/10.1016/j.gloplacha.2021.103614.
Sluijs, A., Schouten, S., Donders, T.H., et al., 2009. Warm and wet conditions in the Arctic region during Eocene Thermal Maximum 2. Nat. Geosci. 2, 777–780. https://doi.org/10.1038/ngeo668.
Speijer, R.P., Pälike, H., Hollis, C.J., et al., 2020. Chapter 28–the Paleogene Period. Geologic Time Scale 2020. Elsevier, pp. 1087–1140. https://doi.org/10.1016/B978-0-12-824360-2.00028-0.
Srivastava, G., Bhatia, H., Verma, P., 2023. High rainfall afforded resilience to tropical rainforests during early Eocene Climatic Optimum. Palaeogeogr. Palaeoclimatol. Palaeoecol. 628, 111762. https://doi.org/10.1016/j.palaeo.2023.111762.
Standardization Administration, China, 2022. Determination for Total Organic Carbon in Sedimentary Rock, GB/T 19145-2022.
Stap, L., Lourens, L.J., Thomas, E., et al., 2010. High resolution deep-sea carbon and oxygen isotope records of Eocene Thermal Maximum 2 and H2. Geology 38, 607–610. https://doi.org/10.1130/G30777.1.
Tanaka, E., Yasukawa, K., Ohta, J., et al., 2022. Enhanced continental chemical weathering during the multiple early Eocene hyperthermals: New constraints from the southern Indian Ocean. Geochem. Cosmochim. Acta 331, 192–211. https://doi.org/10.1016/j.gca.2022.05.022.
Thomas, D.J., Zachos, J.C., Bralower, T.J., et al., 2002. Warming the fuel for the fire: evidence for the thermal dissociation of methane hydrate during the Paleocene-Eocene thermal maximum. Geology 30, 1067–1070. https://doi.org/10.1130/0091-7613(2002)030<1067:WTFFTF>2.0.CO;2.
Thomson, D.J., 1982. Spectrum estimation and harmonic analysis. Proc. IEEE 70, 1055–1096. https://doi.org/10.1109/PROC.1982.12433.
Tissot, B., Welte, D.H., 1984. Petroleum Formation and Occurrence. Springer Verlag, Berlin. https://doi.org/10.1007/978-3-642-87813-8.
Torrence, C., Compo, G.P., 1998. A practical guide to wavelet analysis. B. Am. Meteorol. Soc. 79, 61–78. https://doi.org/10.1175/1520-0477(1998)079<0061:APGTWA>2.0.CO;2.
Turner, S.K., Sexton, P.F., Charles, C.D., et al., 2014. Persistence of carbon release events through the peak of early Eocene global warmth. Nat. Geosci. 7, 748–751. https://doi.org/10.1038/ngeo2240.
Van Krevelen, D.W., 1993. Coal: Typology–Physics–Chemistry–Constitution. Elsevier, Netherlands. https://doi.org/10.5860/choice.31-3793.
Varkouhi, S., Tosca, N.J., Cartwright, J.A., et al., 2024. Pervasive accumulations of chert in the Equatorial Pacific during the early Eocene climatic optimum. Mar. Pet. Geol. 167, 106940. https://doi.org/10.1016/j.marpetgeo.2024.106940.
Vermeer, M., Rahmstorf, S., Clark, W.C., 2009. Global sea level linked to global temperature. Proc. Natl. Acad. Sci. USA 106 (51), 21527–21532. https://doi.org/10.1073/pnas.0907765106.
Wang, D.L., Schwark, L., Ruebsam, W., et al., 2022. Eccentricity paced paleoenvironment evolution and microbial community structure in the Gulf of Mexico during the outgoing Early Eocene Climate Optimum. Earth Planet Sci. Lett. 599, 117857. https://doi.org/10.1016/j.epsl.2022.117857.
Wang, M., Chen, H.H., Huang, C.J., et al., 2020. Astronomical forcing and sedimentary noise modeling of lake-level changes in the Paleogene Dongpu Depression of North China. Earth Planet Sci. Lett. 535, 116116. https://doi.org/10.1016/j.epsl.2020.116116.
Wang, S.F., Dong, D.Z., Wang, Y.M., et al., 2014. Geochemistry evaluation index of redox sensitive elements for depositional environments of Silurian Longmaxi organic-rich shale in the south of Sichuan Basin. Mar. Orig. Pet. Geol. 19 (3), 27–34. https://doi.org/10.14027/j.issn.1000-0550.2022.069.
Wei, W., Algeo, T.J., 2019. Elemental proxies for paleosalinity analysis of ancient shales and mudrocks. Geochem. Cosmochim. Acta 287, 341–366. https://doi.org/10.1016/j.gca.2019.06.034.
Wei, X., Yan, D., Luo, P., et al., 2020. Astronomically forced climate cooling across the Eocene–Oligocene transition in the Pearl River Mouth Basin, northern South China Sea. Palaeogeogr. Palaeoclimatol. Palaeoecol. 558, 109945. https://doi.org/10.1016/j.palaeo.2020.109945.
Wei, X.S., Deng, Y., Yan, D.T., et al., 2023. Organic matter enrichment in Asia's palaeolake controlled by the early and middle Eocene global warming and astronomically driven precessional climate. Mar. Pet. Geol. 154, 106342. https://doi.org/10.1016/j.marpetgeo.2023.106342.
Weisburd, D., Britt, C., Wilson, D.B., et al., 2020. Measuring Association for scaled data: Pearson's correlation coefficient. In: Basic Statistics in Criminology and Criminal Justice. Springer, Cham. https://doi.org/10.1007/978-3-030-47967-1_14.
Westerhold, T., Marwan, N., Drury, A.J., et al., 2020. An astronomically dated record of Earth's climate and its predictability over the last 66 million years. Science 369 (6509), 1383–1387. https://doi.org/10.1126/science.aba6853.
Westerhold, T., Röhl, U., Donner, B., et al., 2018. Global extent of early Eocene hyperthermal events: A new Pacific benthic foraminiferal isotope record from Shatsky Rise (ODP Site 1209). Paleoceanogr. Paleoclimatol. 33, 626–642. https://doi.org/10.1029/2017PA003306.
Wing, S.L., Bown, T.M., Obradovich, J.D., 1991. Early Eocene biotic and climatic change in interior western North America. Geology 19, 1189–1192. https://doi.org/10.1130/0091-7613(1991)019<1189:EEBACC>2.3.CO;2.
Woolway, R.I., Kraemer, B.M., Lenters, J.D., et al., 2020. Global lake responses to climate change. Nat. Rev. Earth Environ. 1, 388–403. https://doi.org/10.1038/s43017-020-0067-5.
Wu, Y.Q., Jiang, F.J., Chen, D., et al., 2023. Influencing mechanism of saline sediments on pore system formation and evolution in terrestrial shales. Pet. Sci. 20, 3280–3300. https://doi.org/10.1016/j.petsci.2023.06.010.
Wu, Y.Q., Jiang, F.J., Xu, Y.L., et al., 2024. Doubthouse climate influences on the carbon cycle and organic matter enrichment in lacustrine basins: Astrochronological and paleontological perspectives. J. Asian Earth Sci., 106155 https://doi.org/10.1016/j.jseaes.2024.106155.
Wu, Y.Q., Jiang, F.J., Xu, Y.L., et al., 2025a. Middle Eocene Climatic Optimum drove palaeoenvironmental fluctuations and organic matter enrichment in lacustrine facies of the Bohai Bay Basin, China. Palaeogeogr. Palaeoclimatol. Palaeoecol. 659, 112665. https://doi.org/10.1016/j.palaeo.2024.112665.
Wu, Y.Q., Hu, T., Jiang, F.J., et al., 2025b. Lacustrine records of Paleocene-Eocene Thermal Maximum (PETM) triggered by volcanic activity. Org. Geochem. 200, 104899. https://doi.org/10.1016/j.orggeochem.2024.104899.
Xiong, L., 2021. Sedimentary characteristics and semi-deep lacustrine facies spatial distribution of Wenchang Formation in Kaiping Sag, China. Offshore Oil Gas 33 (5), 51–61. https://doi.org/10.11935/j.issn.1673-1506.2021.05.006 (in Chinese).
Xiong, L., Xie, X., Zhao, Z., et al., 2021. Distribution prediction of middle-deep lacustrine source rocks in Eocene Wenchang Formation in the kaiping Sag, Pearl mouth Basin. Acta Geol. Sin. Engl. 95 (1), 248–258. https://doi.org/10.1111/1755-6724.14629.
Xu, C.G., Gao, Y.D., Liu, J., et al., 2024a. Discovery of large deep-water and deep-formation oilfield in south kaiping sag of Pear River Mouth basin and new geological under standings. China Offshore Oil Gas 36 (1), 1–13. https://doi.org/10.11935/j.issn.1673-1506.2024.01.001 (in Chinese).
Xu, C.G., Gao, Y.D., Liu, J., et al., 2024b. Discovery of “detachment-core complex type” basins offshore the northern South China Sea and their oil and gas geological conditions: A case study of the Kaiping sag in the northern South China Sea. Earth Sci. Front. 31 (6), 381–404. https://doi.org/10.13745/j.esf.sf.2024.7.1.
Yang, C.H., Zeng, Q.B., Ji, M., et al., 2023. Accumulation conditions and exploration direction of crude oil in detachment rift of kaiping sag in deep water area of Pearl River Mouth Basin. Acta Pet. Sin. 44 (6), 933–947.. https://doi.org/10.7623/syxb202306004 (in Chinese).
Yarincik, K.M., Muray, R.W., Peterson, L.C., 2000. Climatically sensitive eolian and hemipelagic deposition in the Cariaco Basin, Venezuela, over the past 578,000 years: Results from Al/Ti and K/Al. Paleoceanography 15 (2), 210–228. https://doi.org/10.1029/1999PA900048.
Ye, Q., 2019. The Late Mesozoic Structure Systems in the Northern South China Sea Margin: Geodynamics and their Influence on the Cenozoic Structures in the Pearl River Mouth Basin. China University of Geosciences, Wuhan. https://doi.org/10.27492/d.cnki.gzdzu.2019.000072 (in Chinese).
Yin, P., 2024. 100-mln-tonnes of New Oil, Gas Reserves Discovered in South China Sea. Xinhua, 03. https://english.www.gov.cn/news/202403/09/content_WS65ebd1dcc6d0868f4e8e4e60.html.
Yin, S.Y., Lei, C., Ye, J.R., et al., 2024. Constraints of paleoclimate and paleoenvironment on organic matter enrichment in Lishui Sag, East China Sea Basin: Evidence from element geochemistry of Paleocene Mudstones. Earth Sci. 49 (7), 2359–2372. https://doi.org/10.3799/dqkx.2023.011.
Zachos, J., Dickens, G., Zeebe, R., 2008. An early Cenozoic perspective on greenhouse warming and carbon-cycle dynamics. Nature 451, 279–283. https://doi.org/10.1038/nature06588.
Zachos, J., Pagani, M., Sloan, L., et al., 2001. Trends, rhythms, and aberrations in global climate 65 Ma to present. Science 292, 686–693. https://doi.org/10.1126/science.1059412.
Zachos, J.C., Stott, L.D., Lohmann, K.C., 1994. Evolution of early Cenozoic marine temperatures. Paleoceanography 9, 353–387. https://doi.org/10.1029/93PA03266.
Zeng, Y., Chen, J.A., Zhu, Z.J., 2011. Advance and prospective of Rb/Sr ratios in lake sediments as an index of paleoclimate/paleoenvironment. Adv. Earth Sci. 26 (8), 805–810. https://doi.org/10.11867/j.issn.1001-8166.2011.08.0805 (in Chinese).
Zhang, J.A., Jia, Y.L., Shen, H.Y., et al., 2011. Element features in different grain size fractions of lacustrine sediment and their environmental implication: A case study of Huangqihai Lake. Acta Sedimentol. Sin. 29 (2), 381–387. http://ir.isl.ac.cn/handle/363002/1194.
Zhang, L.L., Shu, L.F., Feng, X., et al., 2020. Further discussion on the age assignment of Enping Formation in the Pearl River Mouth Basin. China Offshore Oil Gas 32 (5), 9–18. https://doi.org/10.11935/i.issn.1673-506.2020.05.002 (in Chinese).
Zhang, R., Li, X.J., Xu, Y., 2022a. The 173-kyr obliquity cycle pacing the Asian monsoon in the eastern Chinese Loess Plateau from late Miocene to Pliocene. Geophys. Res. Lett. 49 (2), e2021GL097008. https://doi.org/10.1029/2021GL097008.
Zhang, S.H., Ji, W.Q., Chen, H.B., 2022b. Advances of driving mechanisms of the Early Eocene Climatic Optimum (EECO): Constraints from the Linzizong volcanic rocks in southern Tibet. Acta Petrol. Sin. 38 (5), 1313–1327. https://doi.org/10.18654/1000-0569/2022.05.03.
Zhang, X.T., Peng, G.R., Wang, G.Z., 2022c. Fault response to the Huizhou Movement in the Pearl River Mouth Basin: Insights from a case study of the Eastern

Yangjiang Sag. Farth Sci. Front. 29 (5), 161–175. https://doi.org/10.13745/j.esf.sf.2021.9.24.

Zhang, S.H., Ji, W.Q., Chen, H.B., 2023. Linking rapid eruption of the Linzizong volcanic rocks and Early Eocene Climatic Optimum (EECO): Constraints from the Pana Formation in the Linzhou and Pangduo basins, southern Tibet. Lithos 446–447, 107159. https://doi.org/10.1016/j.lithos.2023.107159.

Zhao, P., Peng, G., Wu, J., et al., 2022. Lacustrine source rock deposition model and main controlling factors of the Wenchang Formation in a small-scale Sag, Zhui Depression, Pearl River Mouth Basin. Acta Sedimentol. Sin. 40 (4), 1109–1121 https://doi.org/10.14027/j.issn.1000-0550.2021.081 (in Chinese).